

JGR Space Physics

RESEARCH ARTICLE

10.1029/2021JA029401

Key Points:

- We present a new index to process break-points and subsequent steepening in plasma density spectra at high latitudes on a systematic basis
- When the E-region conductance is high, there is a strong tendency for spectra to steepen at the scale interval between 40 and 1 km
- There is a tendency for spectra not to steepen near the cusp, where F-region plasma density and turbulence is enhanced

Correspondence to:

M. F. Ivarsen,
m.f.iversen@fys.uio.no









Citation:

Ivarsen, M. F., St-Maurice, J.-P., Jin, Y., Park, J., Miloch, W., Spicher, A., et al. (2021). Steepening plasma density spectra in the ionosphere: The crucial role played by a strong E-region. *Journal of Geophysical Research: Space Physics*, 126, e2021JA029401. <https://doi.org/10.1029/2021JA029401>

Received 3 APR 2021
Accepted 21 JUL 2021

© 2021. The Authors.
This is an open access article under the terms of the [Creative Commons Attribution License](https://creativecommons.org/licenses/by/4.0/), which permits use, distribution and reproduction in any medium, provided the original work is properly cited.

Steepening Plasma Density Spectra in the Ionosphere: The Crucial Role Played by a Strong E-Region

Magnus F. Ivarsen¹ , Jean-Pierre St-Maurice^{2,3} , Yaqi Jin¹ , Jaeheung Park^{4,5} ,
Wojciech Miloch¹ , Andres Spicher⁶ , Young-Sil Kwak^{4,5} , and Lasse B. N. Clausen¹ 

¹Department of Physics, University of Oslo, Oslo, Norway, ²Department of Physics and Engineering Physics, University of Saskatchewan, Saskatoon, SK, Canada, ³Department of Physics and Astronomy, University of Western Ontario, London, ON, Canada, ⁴Korea Astronomy and Space Science Institute, Daejeon, South Korea, ⁵Department of Astronomy and Space Science, Korea University of Science and Technology, Daejeon, South Korea, ⁶Department of Physics and Technology, the Arctic University of Norway, Tromsø, Norway

Abstract Based on the Swarm 16 Hz Advanced Plasma Density data set, and using the Swarm A satellite, we apply automatic detection of spectral breaks in seven million sampled plasma density power spectra in the high-latitude F-region ionosphere. This way, we survey the presence of plasma irregularity dissipation due to an enhanced E-region conductance, caused both by solar photoionization and particle precipitation. We introduce a new quantity named the steepening slope index (SSI) which we use to estimate the occurrence rate of break-points in sampled plasma densities. We provide an interpretation of SSI in the context of solar photoionization-induced conductance enhancements of the E-region. We present a comprehensive climatology of the SSI occurrence rate, along with statistics documenting characteristic high-latitude plasma density spectra. In the absence of steepening, the typical spectral index is 2.1. When density spectra steepen, the index is typically 1.6 at large scales, and 2.7 at small scales. We discuss the impact of high-energy deeply penetrating electron precipitation in the diffuse aurora, and precipitating electrons in the aurora at large. Here, a key finding is that near the cusp, where the F-region conductance is enhanced, spectra tend *not* to steepen. We find that both the diffuse and discrete aurora are modulating F-region plasma irregularity dissipation through an enhancement of E-region conductance, highlighting the role played by factors other than solar zenith angle in high-latitude plasma dynamics. The influence of E-region conductance on spectral shapes indicates the need for a new discussion of how particle precipitation can structure the local winter high-latitude F-region ionosphere.

Plain Language Summary While the growth of turbulent plasma structures in the high-latitude ionosphere has been paid much attention, the dissipation or decay of these structures has evidently not. By analyzing a massive amount of data from the European Space Agency's Swarm mission, we can create a map of turbulent structure decay in the polar and sub-polar regions of Earth. Perhaps surprisingly, we find that turbulence and dissipation in fact go hand in hand. Both extreme ultraviolet radiation from the Sun and energetic particles in the aurora are causing widespread plasma turbulence dissipation.

1. Introduction

The ionosphere, Earth's immediate space environment, is intimately connected to the solar system's greater, continuous plasma environment, the solar wind. Through the solar wind, the ionosphere is injected with energy, in a stream of charged particles (Cowley, 2000; Dungey, 1961). Partially as a consequence of this energy input, plasma instabilities occur in the high-latitude ionosphere, which is the ultimate cause of widespread turbulent structuring, called plasma irregularities (Tsunoda, 1988). On small scales (< 10 km), such ionospheric plasma irregularities cause rapid scintillations in radio signal phase and amplitude, to the general detriment of GPS services (Kintner et al., 2007; Yeh & Liu, 1982).

In the high-latitude regions of the ionosphere, the occurrence of plasma irregularities is in general subject to strong seasonal dependencies, where local winter is accompanied by an increase in observed plasma irregularities (Heppner et al., 1993; Jin et al., 2018, 2019; Prikryl et al., 2015). These seasonal changes are not

only the result of a differing rate of irregularity production, but also the result of plasma diffusion (Ivarsen et al., 2019).

1.1. Diffusion in the High Latitude F Region

Diffusion is to be understood as a transport mechanism that causes plasma structures to dissolve into the surrounding plasma. In the presence of this mechanism, when plasma irregularities (turbulent structures) only undergo diffusion, they *dissipate*. The timescale involved in irregularity dissipation is usually seen in the context of the time it takes a plasma density gradient to decrease to e^{-1} times its initial value (referred to as e -folding time). If diffusion was controlled by molecular processes so as to exhibit a simple response to pressure gradients, one diffusive e -folding time should be given by Vickrey and Kelley (1982),

$$\tau = \frac{1}{k^2 D_{\perp}}, \quad (1)$$

where D_{\perp} is the diffusion coefficient for field-perpendicular plasma structures, and k is the wave number resulting from a Fourier decomposition of the plasma density distribution *in a direction perpendicular to the magnetic field*.

Inside the polar caps, plasma diffusion adheres to the following principles: strongly magnetized electrons are in effect frozen in the magnetic field, leading the motion of the ions to create an ambipolar electric field, which serves to severely retard the ion diffusion. Vickrey and Kelley (1982) (VK82, hereafter) developed a framework to explain the observed seasonal differences in polar cap plasma irregularity occurrences. During local summer, a high E-region conductivity shorts out the ambipolar electric field, causing F-region plasma to diffuse at the high ion perpendicular diffusion rate instead of the balanced ambipolar diffusion rate. Conversely, during local winter, the E-region conductivity can become negligible, causing plasma to diffuse at the slow ambipolar diffusion rate. As a result, VK82 proposed a new diffusion equation, where D_{\perp} in Equation 1 can be expressed as (Ivarsen et al., 2021),

$$D_{\perp} = \frac{\Sigma^E}{\Sigma^F + \Sigma^E} D_{\perp,i}. \quad (2)$$

where $\Sigma_{F,E}$ is the *height-integrated* Pedersen conductivity (i.e., conductance) of the F- and E-region respectively. Also, $D_{\perp,i}$ is the field-perpendicular *ion* diffusion coefficient. In other words, the ratio of E-to F-region Pedersen conductance controls high-latitude F-region plasma diffusion. Nevertheless, Ivarsen et al. (2021) also concluded that although the mechanisms causing Equation 2 are taking place, the k^{-2} scaling in Equation 1 is evidently not correct: the lifetimes of turbulent plasma structures are longer than expected from theoretical molecular diffusion considerations. In effect, the findings presented by Ivarsen et al. (2021) lead to the conclusion that Equation 1 is not taking into account all the relevant physical processes at play. However, it can be shown that even when the diffusion operator is not associated with molecular pressure gradients, Equation 2 is still valid, where $D_{\perp,i}$ now is to be understood as an operator controlled by *turbulence*. E-region Pedersen conductance then remains a key ingredient in high-latitude plasma diffusion.

Changes in ionospheric Pedersen conductance are broadly predicted by changes in solar extreme-ultraviolet (EUV) photoionization, and by proxy, solar zenith angle (SZA, the angle between a vector normal to Earth's surface and the Sun). SZA is a strong predictor for Pedersen conductance (Brekke & Moen, 1993; Fujii et al., 1981; Ridley et al., 2004; Vickrey et al., 1981). For high values of SZA, in the absence of EUV photoionization, ionospheric conductivity is strongly affected by precipitating electrons (Vickrey et al., 1981). In fact, overall, the particle energy of individual precipitating electrons is higher during local winter and in darkness (Liou et al., 2001; Newell et al., 2010). Thus, the flux of highly energetic auroral precipitation exhibits opposite seasonal behavior to that of EUV photoionization. Pedersen conductivity consequently does not exhibit strong seasonal dependencies in the auroral zone E-region (Kwak & Richmond, 2007), where deeply penetrating electrons assure that both Pedersen and Hall conductances remain relatively high regardless of solar EUV photoionization (Robinson et al., 2021). When SZA is not in control of E-region conductance, the aurora then steps in.

Returning to diffusion, plasma structure dissipation in the auroral zone will then not adhere to a simple dependence on incident solar photoionization. Since we cannot under any circumstance assume an absence

of irregularity production sources, plasma structures here are generated through instability processes, meaning that they will undergo simultaneous growth and dissipation (Huba et al., 1985; Tsunoda, 1988). To complicate matters, strong plasma turbulence can accelerate the return to equilibrium by creating enhanced mixing, resulting in a drastically increased diffusion coefficient (Braginskii, 1965; Kaufman, 1990). Conversely, free energy can push a blob of plasma toward instability without ever making it unstable, which would increase the decay time of stable plasma. As a direct consequence of electron precipitation, the auroral region shows an abundance of plasma irregularities (Kelley et al., 1982), which may be the cause of widespread GPS scintillations (Hong et al., 2020; Prikryl et al., 2015).

1.2. Turbulent Spectral Shapes

Turbulent structuring is readily scrutinized using a powerful tool, the power spectral density (PSD) analysis. The power spectrum, $S(f)$, of a plasma density timeseries is a measure of the strength of fluctuations in the observed plasma density at a given frequency f . When the timeseries is measured using an orbiting spacecraft, and assuming that the spacecraft velocity is much greater than the local plasma velocity, $S(f)$ can be used as an estimator for spatially distributed fluctuation strength. In other words, the distribution of power on the frequency spectrum reflects the intensity of fluctuations on a range of *spatial scales* λ , through $\lambda = v_S / f$, where v_S is the spacecraft velocity (around 7.6 km s⁻¹ in the topside F-region). Power spectra measured in high-latitude ionospheric plasma density fluctuations can often be described by a power law (Mounir et al., 1991; Phelps & Sagalyn, 1976; Spicher et al., 2014; Tsunoda, 1988),

$$S(f) \propto f^{-\alpha}, \quad (3)$$

where α is a positive number. As it happens, plasma density power spectra often display a break-point, or a knee, in $S(f)$. The presence of such a break-point in Equation 3 leads to,

$$S(f) \propto \begin{cases} f^{-\alpha_1}, & \text{for } f \leq f_b, \\ f^{-\alpha_2}, & \text{for } f \geq f_b, \end{cases} \quad (4)$$

where $\alpha_{1,2}$ represents the initial and second slopes, or spectral index, for the low- and high-frequency ranges respectively and where f_b is the frequency at the break point where the spectral slope changes from α_1 to α_2 .

The literature is full of examples of spectra undergoing steepening at a spectral break point, namely break-points at which $\alpha_2 > \alpha_1$ (Kelley, 1989a). Using a very large data set acquired with the high-resolution (16 Hz) in-situ plasma density data from the Swarm mission (Friis-Christensen et al., 2006; Knudsen et al., 2017), we have set out to investigate spectral steepening in the F region near 450 km altitude in terms of where and when it happens and at what wavelength it occurs in a 1–100 km interval. A primary motivation for this study is that the origin of steepening spectra has been blamed on a variety of notions that could benefit from some sorting out. For instance, steepening has been associated with transitions from an inertial regime to a fully collisional regime (Keskinen & Huba, 1990). Other studies have interpreted the occurrence of steepening to mean that there is ongoing plasma irregularity dissipation below the scale of the break-point (Kivanc & Heelis, 1998). Moreover, it has been pointed out that break-points at scales between 1 and 10 km coincide with the scale of the F-region ion skin depth (Ivarsen et al., 2019), that is, to say, to plasma instabilities due to transverse electromagnetic perturbations associated with the ion skin depth (Califano et al., 2002; Stenson et al., 2017). The ion skin depth, or ion inertial scale, is defined as $L_i = c / \Omega_{pi}$, where c is the speed of light and Ω_{pi} is the ion plasma frequency. In effect, these instabilities could in turn lead to an *injection* of energy on scales around the break-point. Alternately, in the context of energy injection where turbulent cascade would be in control, the initial spectral index should theoretically adhere to $\alpha_1 = 5 / 3$ until steepening occurs at some scale associated with molecular or other processes (Kintner & Seyler, 1985; Mounir et al., 1991).

Direct irregularity dissipation and energy injection then constitute two interpretations of steepening plasma density spectra. However, energy injection through instabilities at the break-point scale would lead to an accelerated return to equilibrium, and thus cause diffusion (St-Maurice & Hamza, 2009). In other words, the two interpretations go hand in hand. In addition, there is no direct way to distinguish between the two interpretations of a spectral break (Mounir et al., 1991). Natural variability in spectral indices ensures that a strict test of $\alpha_1 = 5 / 3$ for individual spectra is untenable. Nevertheless, spectral breaks in density power

spectra have been found in multiple studies of the high-latitude ionosphere (Basu et al., 1990; Mounir et al., 1991; Spicher et al., 2014; Villain et al., 1986). The interpretations of the spectral breaks found in these studies reflect the ambiguity between the two opposing break-point interpretations.

The above notwithstanding, a key finding from the recent study by Ivarsen et al. (2021) quoted above has been that the lifetime of 10-km scale structures in the F region is strongly affected by the E region electrical conductivity lower down, as predicted by VK82. An implication of the short-circuiting of the electrostatic structures generated in F-region should therefore be that for plasma structures of certain perpendicular scales, ambipolar diffusion should take over the final evolution of the structures in time. In other words, the presence of a strong E-region induced conductance has to introduce an increase in the dissipation rate of structures. This increase should in turn be seen through a spectral break in the spectrum at some high enough frequency, at least in structures that are large enough to map into the E-region. This has therefore been one of the factors that we have paid attention to in our study of spectral steepening.

Specifically, the present study is a direct follow-up to two previous investigations by Ivarsen et al. (2019) and Ivarsen et al. (2021). In the former, we developed an automatic detection of break-points in plasma density spectra. We applied this in the polar caps to show that SZA is a powerful indicator for the presence of steepening spectra in the polar caps. In the latter, we showed that the lifetimes of diffusing plasma structures in the polar cap (Equation 1) could be explicitly calculated from the plasma-convection estimated using satellite orbits along the noon-midnight meridian. A key finding, we determined that diffusion is faster when there is a strong E-region conductance, and that the ratio $\Sigma_E / (\Sigma_E + \Sigma_F)$ plays a role similar to that predicted by VK82. However, as mentioned above, something is increasing the structure lifetimes by modifying the predicted k^{-2} scaling. We hypothesize that this increase is caused by turbulent velocity fields, inhibiting dissipation. Thus, in the present study, we will investigate the shape of plasma density spectra at high latitudes. If turbulent velocity fields are in control, this should be detectable at larger scales in density spectra. If this is correct then, an enhancement in E-region conductance should be accelerating plasma diffusion, implying that density spectra should exhibit break-points and subsequent steepening, as long as the scales undergoing diffusion are covered by the PSD analysis. While a combination of irregularity source dependencies and diffusion can modify the spectral shapes accordingly, our investigations lead us to posit that there is widespread co-occurrence between the two. As we show in the present publication, we did detect an abundance of break-points with steepening in density spectra, in support for the VK82-style shorting mechanism occurring throughout the sunlit high-latitude F-region ionosphere, as well as in deeply penetrating particle precipitation regions in deep darkness. Our results highlight the need to take particle precipitation-induced irregularity dissipation into account when considering high-latitude F-region plasma irregularities.

2. Methodology

For this study we have used the high-resolution (16 Hz) in-situ plasma density data set from the Swarm mission (Friis-Christensen et al., 2006; Knudsen et al., 2017). We collected data from all Swarm A orbits as they passed through the polar regions (poleward of $\pm 55^\circ$ magnetic latitude [MLAT]) between October 15, 2014 and January 15, 2021, constituting more than 6 years of more or less continuous data coverage (small daily gaps and a few longer-term gaps exist in the data). To calculate MLAT and magnetic local time (MLT), we used the altitude adjusted corrected geomagnetic coordinates system (Baker & Wing, 1989). Next, we sampled 60 s (approximately 456 km) intervals of ionospheric plasma, with a cadence of 5 s before subjecting each 60 s segment to a PSD analysis.

It proves important here to provide some details regarding the analysis to which we subject each 60 s segment of plasma density observations. The approach we chose is analogous to the method presented in Ivarsen et al. (2019). For the PSD itself, we use a variant of Welch's power spectral density (Welch, 1967), consisting of averaged modified periodograms over a logarithmically spaced spectral range (Trbs & Heinzel, 2006). Next, to fit Equation 4 to each spectrum, we use a piecewise linear Hermite function, as documented in D'Errico (2017). This way, we automatically locate the position of a spectral break. If a spectrum exhibits a numerical difference between α_1 and α_2 such that $\alpha_2 - \alpha_1 > 0.8$, we infer a spectral break, and the spectrum is characterized as a *steepening slope* spectrum. If the analyzed spectrum does not exhibit a spectral break,

the numerical difference between α_1 and α_2 , $|\alpha_2 - \alpha_1|$, is lower than 0.8, and we conclude that the analyzed spectrum is adequately described by a single power law (Equation 3). In addition, we require for the spectral break to be found between frequencies of 0.19 and 6.5 Hz, corresponding to spatial scales between 1.2 and 39.9 km, respectively. The reason for this comparatively narrow interval is directly related to the PSD analysis itself—extensive use of window functions in calculating the PSD causes power to diminish in the lowest frequencies. This stated, the interval encompasses both the transitional scale to a fully collisional regime, 2–3 km (Keskinen & Huba, 1990), and the F-region ion skin depth, 2–5 km (Ivarsen et al., 2019). The parameters of our algorithm, such as the 0.8 threshold for steepening spectra were determined through extensive testing, with the central goal in mind: to automatically determine whether there is a natural visual break in the power spectra, which is the criterion generally used for identifying spectral breaks in the literature.

It should be mentioned that we found a few instances of spectra that exhibited some shallowing after a spectral break (e.g., the spectrum in panel E-a in Figure 1). There are a number of possible interpretations of such spectra. They can, for example, be associated with a noise floor in the Swarm 16 Hz density power spectra, which is situated around $S(f) \approx 10^3 \text{ cm}^{-6}/\text{Hz}$ (Ivarsen et al., 2019). Another interpretation of spectra such as the one shown in panel E-a is that the PSD has steepened on scales larger than the interval available to scrutiny in the present study, though this would entail a break-point on scales comparable to the spatial extent of polar cap patches. Strengthening such an interpretation is the relative steepness of the spectral index before the break-point (2.7), compared to typical single-slope spectra (panel E-b). As a counterpoint to such an interpretation is that shallowing spectra overwhelmingly appear in smooth sub-auroral plasma, as is apparent in panel (A). However, as the present study is concerned with spectra that steepen within the scale-interval available for scrutiny, we will not deal here with the rather rare occurrence of high latitude shallowing spectra, other than to conclude that they do not exhibit spectral steepening in the present scale interval.

As mentioned, we collected orbits made by Swarm A crossing both polar regions poleward of $\pm 55^\circ$ MLAT, thereby covering a much larger region than Ivarsen et al. (2019). In addition to the analysis outlined, we also calculated the SZA adjusted for the approximate altitude of the E-region peak, at 110 km.

The end result of this analysis is a binary time series equal to either 0 or 1, which indicates whether the sampled 60 s, or 456 km stretch of F-region plasma, exhibits a spectral break. We call this timeseries the steepening slope index (SSI). Figure 1 shows a typical polar region crossing, which occurred through the northern polar region on December 12, 2017. Panel (A) shows the 16 Hz plasma density, and panels (B–D) document the resulting steepening slope spectra encountered in the interval. Panel (B) shows the first and second spectral indices, α_1 and α_2 , along with the degree with which the spectra are steepening. Panel (C) shows the location of the spectral breaks, and panel (D) shows the SSI, along with a 30-s along-orbit SSI occurrence rate, SSI30s. The latter corresponds to the probability that plasma sampled in a relatively long stretch of Swarm orbit will exhibit a spectral break, as each of the 6 spectra included in the 30 s interval contains contributions from a 456 km stretch of orbit. In the bottom panels (E), we show three examples of spectra, labeled (a, b, and c), where each label is highlighted in a particular spectrum in panel (D). Here, (a) shows a shallowing spectrum, (b) shows a single slope spectrum, and (c) shows a steepening slope spectrum. In all three cases, the values of the slopes are indicated above the plot.

In Figure 1, we see that Swarm A enters the northern polar region from the post-midnight sector at around 15:52:00 UT on December 12, 2017. Poleward of $\sim 65^\circ$ MLAT, it encounters three density enhancements, accompanied by moderate increases in the SSI30s. Although SSI occurrences are associated with the density enhancements, smaller fluctuations in the measured plasma density also register SSI occurrences. As the satellite orbits equatorward through the afternoon sector, it encounters a large enhancement in density and density fluctuations at around $\sim 80^\circ$ MLAT, accompanied by a marked increase in SSI occurrences. On the sharp edges of density enhancements, break-points have a tendency to be found at smaller scales, around 2–3 km. SSI occurrence quickly subsides as the satellite orbits equatorward of $\sim 70^\circ$ in the post-noon sector.

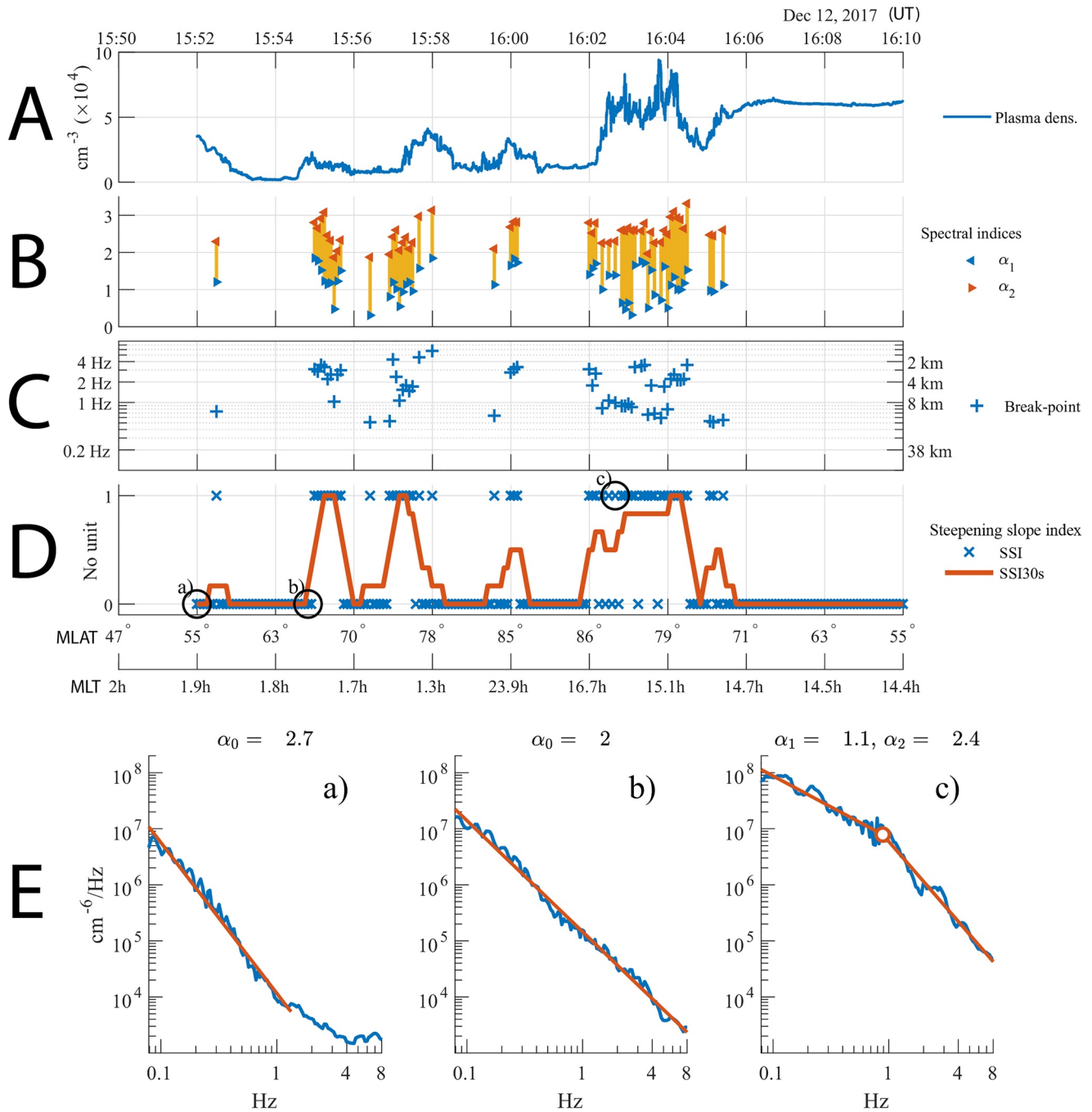


Figure 1. A sample orbit across the northern polar ionosphere, made around 16:00 UT on December 12, 2017. Panel (A) shows the plasma density. Panel (B) shows the first and second spectral indices, α_1 and α_2 , as orange and blue triangles respectively. The extent of the yellow bar connecting the triangles represents the degree with which the slopes of the spectra are steepening. Panel (C) shows the location of the spectral breaks, for frequency (left y-axis) and spatial scale (right y-axis). Panel (D) shows the steepening slope index (SSI) and the SSI30s (a 30-s along-orbit SSI occurrence rate). In panel (E), three examples of spectra are shown, with labels corresponding to specific points in panel (D). The orbital time is indicated in the top x-axis of panel (A), while the position in magnetic latitude (MLAT) and magnetic local time (MLT) is indicated by the two x-axes below panel (D).

3. Results

We aggregated all polar region orbits made by Swarm A between October 14, 2014 and January 15, 2021, giving us a database of roughly seven million plasma density spectra, more or less equally divided between the northern and southern hemispheres. Each spectrum is described by either a single slope ([a] and [b] in

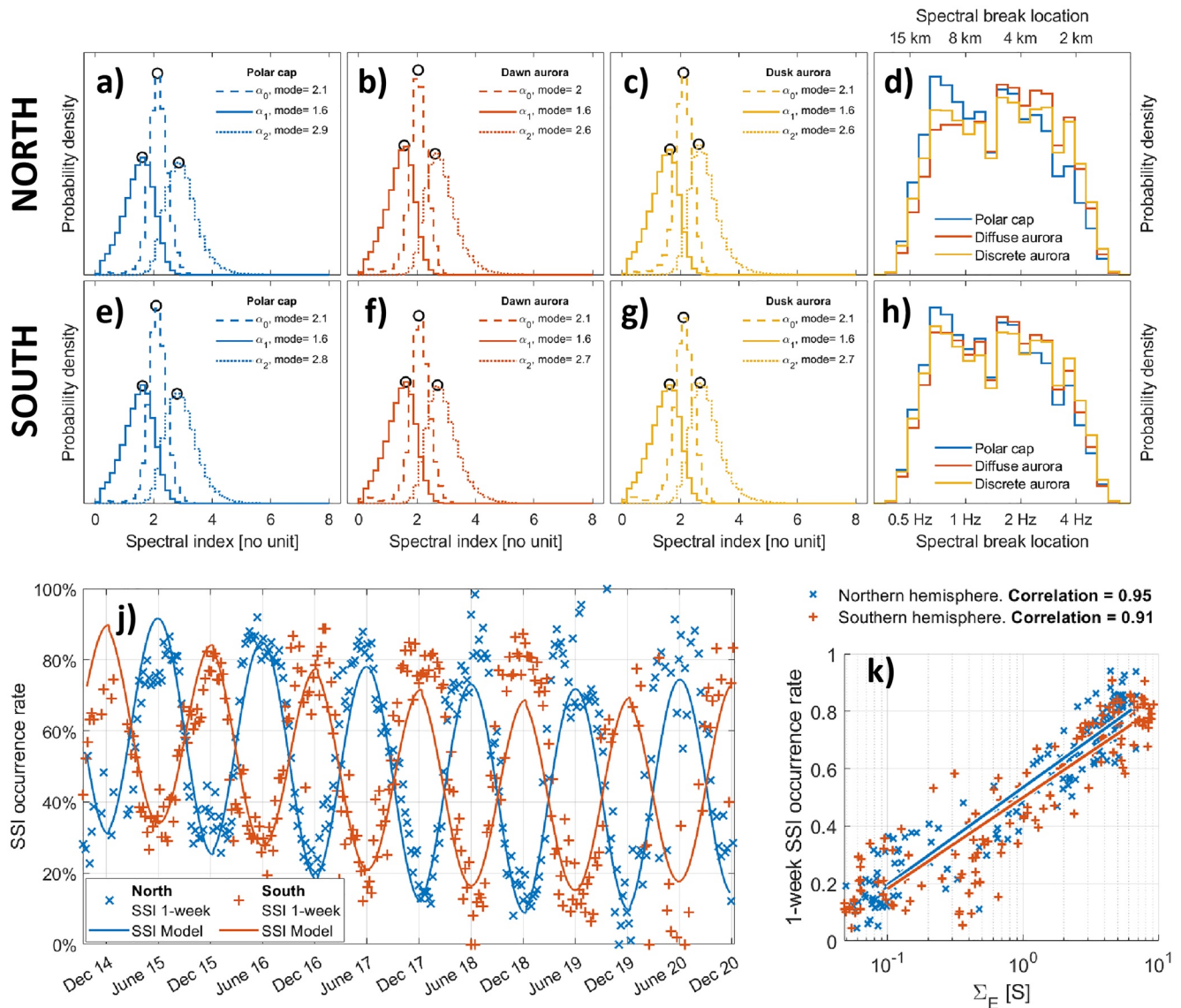


Figure 2. Steepening slope statistics. Panels (a–c) and (e–g) distributions of the first (solid line) and second (dotted line) spectral indices for steepening spectra. Also shown is the distribution of indices for which steepening was not identified (dash line). Panels (a–c): northern hemisphere data. Panels (e–g): southern hemisphere data. Panels (a and e) are for the polar caps (poleward of $\pm 82^\circ$ MLAT). Panels (b and f) are for the diffuse aurora ($63^\circ < |\text{MLAT}| < 75^\circ$, $\text{MLT} < 10$ (h)), while panels (c and g) are for the discrete aurora ($65^\circ < |\text{MLAT}| < 77^\circ$, $\text{MLT} > 14$ (h)). Each distribution is normalized (using estimated probability density values). The mode (peak) of each distribution is indicated, as calculated from a kernel estimation of the probability density distributions. Panels (d, northern hemisphere) and (h, southern hemisphere) show the distributions of the spectral break locations, for the three regions defined, with frequencies (bottom x -axis) and corresponding spatial scale (top x -axis) indicated. Panel (j) shows the long-term development of the polar cap steepening slope index (SSI) occurrence rate. Each data point represents a running 1-week SSI occurrence rate inside the polar caps (poleward of $\pm 82^\circ$ MLAT), where the northern and southern hemispheres are shown in blue and orange respectively. The solid lines are linear fits of SSI against solar zenith angle (SZA), including a slowly varying solar cycle-based trend. The December and June solstices are indicated on the x -axis of panel (j). Panel (k) scatter plot of the 1-week polar cap SSI occurrence rate against the E-region conductance (Σ_E) for both hemispheres, and with the Pearson correlation coefficient between the logarithm of Σ_E and 1-week SSI occurrence rate indicated above the plot. The conductance Σ_E is calculated using global ionospheric models (Bilitza et al., 2014; Bilitza & Reinisch, 2008; Picone et al., 2002; Thult et al., 2015).

Figure 1), or a steepening slope ([c] in Figure 1). Note that the results are not fundamentally different if the analysis is applied to data from Swarm B or C.

In Figure 2, we show various statistics of all the high-latitude aggregated steepening slope spectra. In panels (a–c, for the northern hemisphere) and (e–g, for the southern hemisphere), we show the distribution in

the first (solid lines) and second (dotted lines) spectral indices, $\alpha_{1,2}$ in Equation 4. The separation of order 1.0 between the two distributions is consistent with our choice of 0.8 as a selection criterion for steepening spectra. In addition, we show the distribution of α_0 , the spectral index of slopes where no spectral break could be determined (dashed lines). We show the indices for the polar caps (panels a and e), for the dawn aurora (panels b and f), and for the dusk aurora (panels c and g). Here, we define the polar caps as the area poleward of $\pm 82^\circ$ MLAT, the dawn aurora as the area confined by $63^\circ < |\text{MLAT}| < 75^\circ$, $\text{MLT} < 10$ h, and the dusk aurora as the area confined by $65^\circ < |\text{MLAT}| < 77^\circ$, $\text{MLT} > 14$ h. In panels (a–c) and (e–g), the mode (peak) of the distributions are indicated, where we fit a non-parametric Kernel distribution to the data in order to estimate the exact probability density distributions. Panels (d and h) show the distributions of the location of spectral break points, for all three regions. Here, we find no clear peaks in the distributions, though a dual mode distribution could be inferred.

In panel (j) of Figure 2, we show the long-term development of the polar cap SSI occurrence rate. Each datapoint represents a running 1-week SSI occurrence rate inside the polar caps (poleward of $\pm 82^\circ$ MLAT), where the northern and southern hemispheres are shown in blue and orange respectively. The solid lines are linear fits of SSI against SZA, with a solar cycle-based trend added:

$$p(Z, t) = p_{\text{SZA}}(Z) + p_{\text{SC}}(t), \quad (5)$$

where p is the modeled long-term SSI occurrence rate, p_{SZA} is a linear fit of SSI against SZA, Z represents SZA, and $p_{\text{SC}}(t)$ is a slowly varying solar cycle-based trend, as a function of time t . See appendix A for details about the model parameters.

Panel (k) of Figure 2 provides a final illustration of the strong relation between E-region conductance and polar cap SSI occurrence rates. To this goal we have used E-region conductance values (Σ_E) for a period from 2017 through 2019, based on global ionospheric models, after Ivarsen et al. (2021), and references therein. As is readily observed, the correlation between Σ_E and 1-week polar cap SSI occurrence rates is unambiguous, with Pearson correlation coefficients of 0.95 and 0.91, for the northern and southern hemispheres respectively.

In panels (a through f) in Figure 3, we show a climatology of the occurrence rate of steepening slope spectra. This is calculated based on a spatial binning in MLAT and MLT, where each bin roughly covers the same geographical area. In each panel, the SSI occurrence rate is shown to the left, while the sampled SZA is shown to the right. Moreover, in each panel, magnetic noon (12 h) points toward the location of the Sun, and magnetic dawn (6 h) and dusk (18 h) are situated to the right and left respectively. The SSI occurrence rate is simply the number of spectra exhibiting a double slope divided by the total number of spectra in each bin, while the SZA is the median SZA of that bin. Panels (a, c, and e) show the northern hemisphere, while panels (b, d, and f) show the southern hemisphere. Each panel contains data from a local season. Local summer and winter are defined as 131-day periods centered on both solstices, while equinox is the combined 52-day periods centered on both equinoxes—this way, all days of the year are assigned to a season. Note that the Swarm satellites cover all magnetic local times in a period of 131 days, meaning each local time contains contributions from each year. Panels (a and b) show local summer, panels (c and d) show combined equinoxes, while panels (e and f) show local winter.

We see that inside the polar cap in Figure 3, the SSI occurrence rate shows a predictable behavior with respect to local season. The local winter polar caps exhibit an overall occurrence rate of 28% and 30% for the northern and southern hemispheres respectively, with the corresponding rates being 79% and 74% for the northern and southern local summer polar caps, which is reflected in panel (j) of Figure 2. During local summer, the entire high-latitude regions exhibit a SSI occurrence rate of $> 70\%$, and are stretching equatorward to around magnetic latitudes of $\pm 65^\circ$. During local winter, auroral magnetic latitudes ($65^\circ < |\text{MLAT}| < 75^\circ$) remain regions of high SSI occurrence rate, exhibiting rates in excess of 60%. In both hemispheres, a maximum appears in the morning sector, where the SSI occurrence rate is still in excess of 70% for the northern hemisphere. At auroral latitudes, there are local minima in the SSI occurrence rate distributions in the pre-midnight sector and the noon sector. For all seasons, in both hemispheres, the cusp region ($\sim \pm 75^\circ$ MLAT, 12 h MLT) does not exhibit a clear enhancement in SSI occurrence.

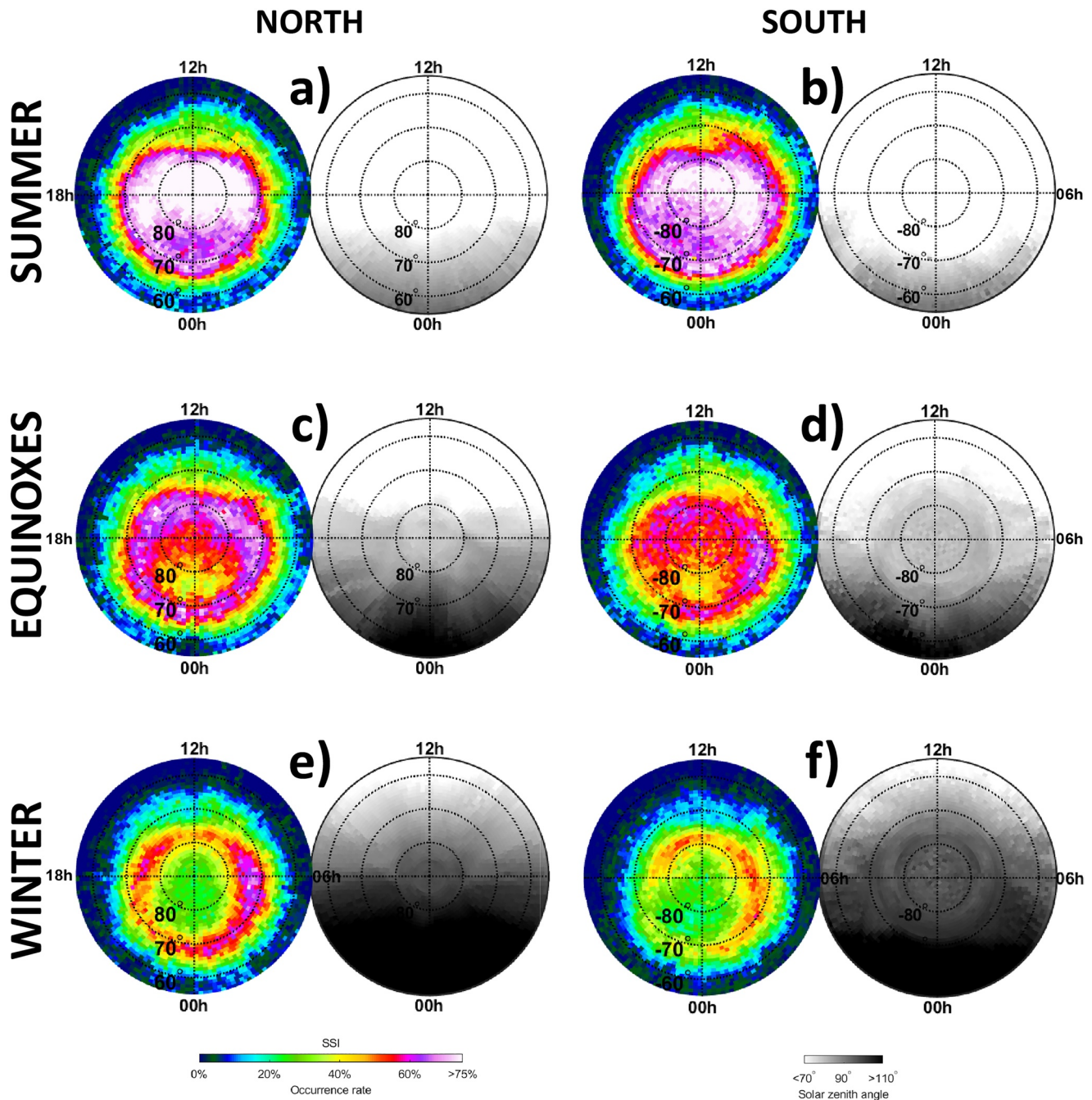


Figure 3. SSI occurrence rate climatology the high-latitude F-region ionosphere (poleward of $\pm 55^\circ$ MLAT). Panels (a, c, and e) display the northern hemisphere, and panels (b, d, and f) display the southern hemisphere. Panels (a and b) show local summer, panels (c and d) show combined equinoxes, while panels (e and f) show local winter, where local summer and winter are defined as 131-day periods centered on both solstices, while equinox is the combined 52-day periods centered on both equinoxes. In all panels, magnetic noon (12 h) points toward the location of the Sun, and magnetic dawn (6 h) and dusk (18 h) are situated to the right and left respectively. Steepening slope index (SSI) occurrence rate is shown to the left in each panel, while median sampled solar zenith angle (SZA) is shown to the right, with colorscales indicated below. Note that the color white in the SSI occurrence rate climatologies signifies a saturation in the colorscale, and not a lack of datapoints.

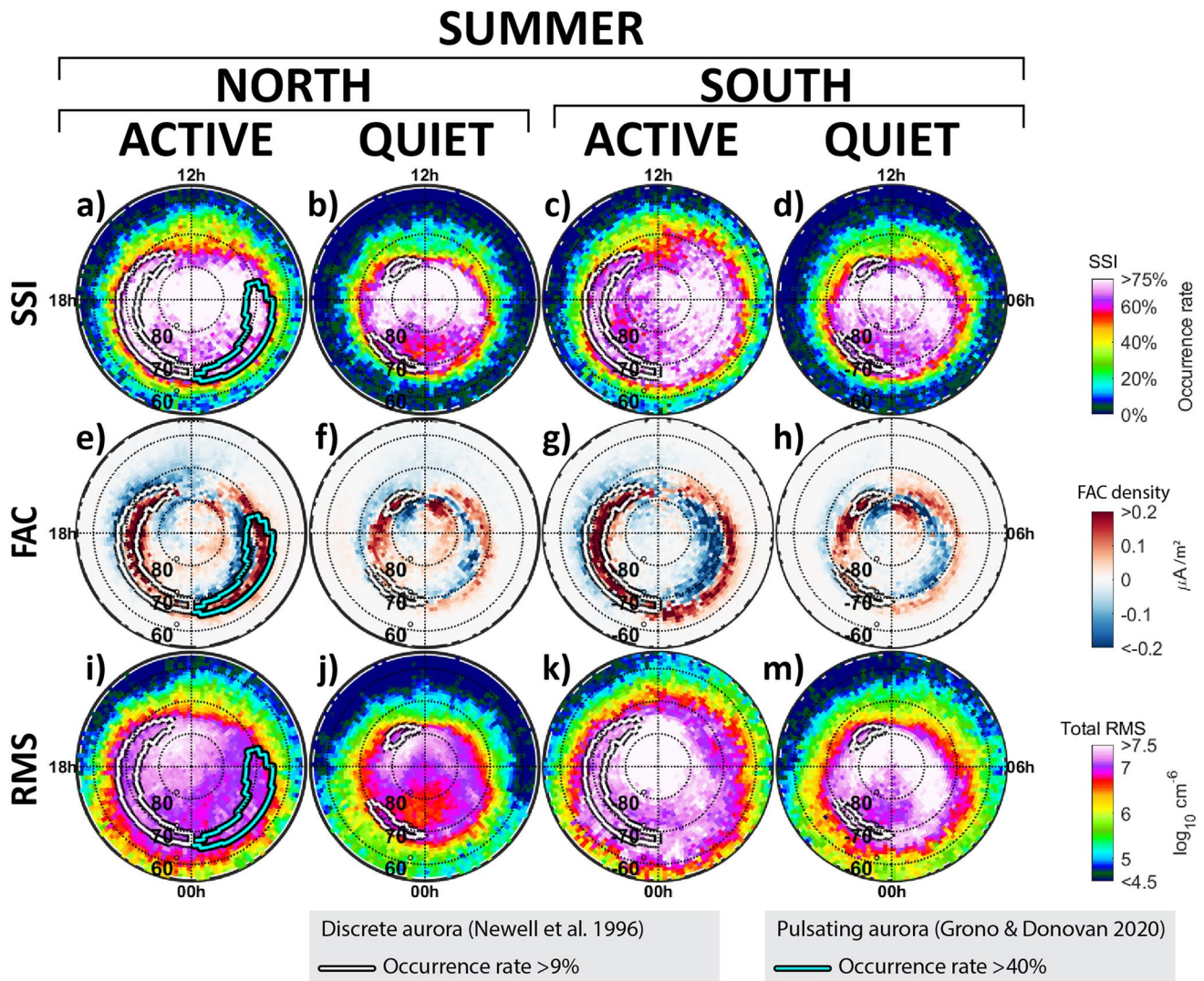


Figure 4. Aggregated data for local *summer*, where summer is defined as a 131-day period centered on the respective summer solstice. We show steepening slope index (SSI) occurrence rates (panels a through d), field-aligned current (FAC) density (panels e through h), and plasma structuring root-mean-square (RMS, panels i through m), for both hemispheres, and for geomagnetically active and quiet times, where we use the SME index to distinguish between the two (Gjerloev, 2012). In the FAC density, red (positive) density denotes a current going upwards, and blue (negative) density denotes a current going downwards. The first and second columns show the northern hemisphere, while the third and fourth columns show the southern hemisphere. In all panels, we show the average distribution of the discrete aurora, based on Newell et al. (1996). In panels (a, e, and i), we show the average distribution of the pulsating aurora, based on Grono and Donovan (2020). Note that the color white in panels (a-d) and (i-m) signifies a saturation in the colorscale, and not a lack of datapoints.

Returning to the median SZA values in the right side of each panel in Figure 3, we see that the regions of very high SSI occurrence rate ($> 70\%$) are the high MLAT—low SZA regimes. In darkness, SSI occurrence rate quickly diminishes, starting with the midnight sector of the equinox polar caps (poleward of $\sim \pm 82^\circ$ MLAT). However, during local winter, there is a clear holdout of consistently high SSI occurrence rate in the auroral region ($65^\circ < \text{MLAT} < 75^\circ$).

To further explore the nature of the results presented in Figure 3, we present in Figures 4 and 5 a climatology of SSI occurrence rate compared to the distribution of field-aligned current (FAC) densities (panels e through h), and to the F-region plasma structuring (panels i through m). For the former, we use the Swarm FAC density data set, which derives FAC density from the perpendicular magnetic field components. To estimate plasma structuring, we use total integrated power from each plasma density spectrum. Total integrated power, given a stationary process, corresponds to the root-mean-square (RMS), or variance σ^2 . We define this quantity as,

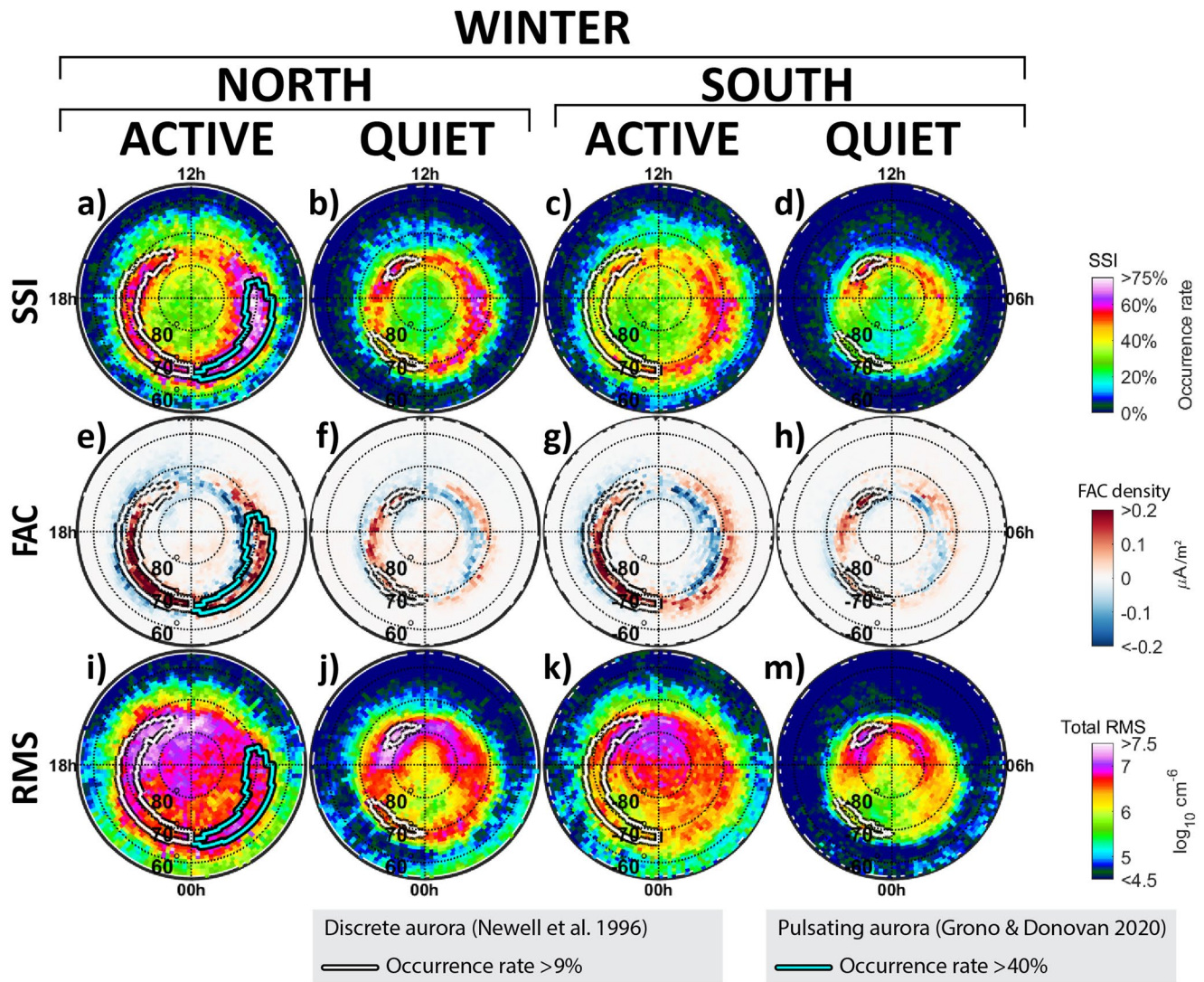


Figure 5. Same as Figure 4, but for local winter.

$$\sigma^2 = \int_{0.3\text{Hz}}^{8\text{Hz}} S(f)df, \quad (6)$$

where the limits of the integration reflect the scale interval under scrutiny in the present study. The RMS has units cm^{-6} and reflects the total power of plasma density fluctuations present in each sampled 60 s segment. In Figure 4 (local summer) and Figure 5 (local winter), we show SSI occurrence rate along the first row (panels a through d), FAC density along the second row (panels e through h), and the logarithm of RMS along the third row (panels i through m). The values in the distributions of FAC density and RMS are taken as the median in each bin, where each bin contains the same data coverage as the corresponding bins of SSI occurrence rate. Positive values of FAC density correspond to an upwards current direction in both hemispheres. We further divide the data into geomagnetically active and quiet times. Here, we use the SME index from the SuperMAG initiative (Gjerloev, 2012), which is a ground-based alternative to the AE index (Davis & Sugiura, 1966). The SME index is a direct indicator of the nightside integrated auroral power (Newell & Gjerloev, 2011), and has the added benefit that it extends to December 31, 2019, which is roughly two years longer than the AE index. Specifically, we label as active times when the SME index is higher than its median value, and quiet as times when the SME index is lower than its median value. Note that in using

the SME index to separate our data into geomagnetically active and quiet times, we exclude the last year of Swarm data from Figures 4 and 5.

To visualize the extent of the aurora, we show as an overlay the area from which the pulsating aurora had an occurrence rate in excess of 40%, based on a recent climatology of pulsating aurora in the northern hemisphere, presented in Grono and Donovan (2020). Using all-sky cameras with a data coverage from 2006 to 2016, the latter study surveyed several subcategories of pulsating aurorae, of which we show the most prevalent type, the amorphous pulsating aurora. Note that Grono and Donovan (2020) did not take geomagnetic conditions or local season into account, but we posit that the visual appearance of the aurora is most prevalent during local winter in geomagnetically active times (Newell et al., 2010), and so we only overlay the pulsating aurora distribution over the northern hemisphere active climatologies (panels a, e, and i in both Figures 4 and 5). Then, we overlay the distribution of discrete aurora energy flux from Newell et al. (1996). The latter study presented a climatology of the discrete aurora, using precipitation data from the DMSP satellites, with a data coverage lasting from December 1983 to November 1992. The discrete aurora climatology is echoed by Liou et al. (1997), who measured optical UV emissions. In all panels in Figures 4 and 5, we show the regions of discrete aurora occurrence rate greater than ~9% as a white line. Newell et al. (1996) divided observations into active and quiet times by the north-south component of the interplanetary magnetic field (IMF), compared to our division using the SME index. However, active times as defined using the SME index occur on average during times of southward IMF, and vice versa for quiet times. As a note to the drastically differing magnitudes of the occurrence rates between Newell et al. (1996) and Grono and Donovan (2020), we believe this is due to differing methodologies. The former calculated occurrence rates based on all sampled data, while the latter calculated occurrence rates only from all-sky images that were clear.

In Figure 4, which shows local *summer* conditions, the SSI occurrence rate distributions (panels a through d) are not drastically different between active and quiet times, nor between hemispheres, with consistently high occurrence rates (>70%) across the high-latitude ionospheres. The region of high occurrence rate moves equatorward during active times, and the cusp regions (poleward of $\pm 75^\circ$ MLAT, 12 h MLT) does not exhibit any enhancements in SSI occurrence rate. The FAC density data (panels e through h), shows the FAC flowing into (blue) and out of (red) the high-latitude ionosphere. In the plasma structuring data (RMS, panels i through m), we see stark differences both between active and quiet times, and between hemispheres. In the sunlit northern hemisphere, plasma structuring peaks near the cusp region and stretching into the post-noon sector. We observe regions of enhanced structuring in the large-scale polar cap convection path. In the nighttime northern hemisphere, regions of enhanced plasma structuring are co-located with the distributions of discrete and pulsating aurora, both in geomagnetically active and quiet times. In the southern hemisphere, the same pattern is discernible, but with much stronger enhancements in structuring, and with nightside enhancements reaching further equatorward than in the northern hemisphere.

In Figure 5, which shows local *winter* conditions, the SSI occurrence rate distributions (panels a through d) exhibit a clear dependence on the SME index. Furthermore, regions of enhanced SSI occurrence rate (>60%) are strongly co-located with the distributions of discrete and pulsating aurora, both during geomagnetically active and quiet times. The dawn side auroral SSI occurrence rates are noticeably higher than on the dusk side. Furthermore, as during local summer, the cusp regions do not exhibit elevated SSI occurrence rates. The distributions of FAC density during local winter are similar to local summer, but weaker, reflecting the relationship between FAC strength and solar illumination (Yamamoto et al., 2003).

4. Discussion

4.1. Spectral Indices and Their Relation to Geophysical Conditions

The top eight panels of Figure 2 all reflect the general characteristics of the plasma density spectra identified by Swarm A. The distributions of the first spectral index of the steepening spectra, α_1 , clearly peaks at $\alpha_1 = 1.6$ for all three regions considered, and in both hemispheres. The second spectral index tends to come in at $\alpha_2 \approx 2.7$, with the polar caps showing slightly steeper α_2 . The spectra best described by a single slope exhibit a spectral index of 2.1, which is in between the average values of α_1 and α_2 . For steepen-

Table 1
The Point Biserial Correlation Coefficient Between SZA and the Binary Variable SSI, for the Three Regions Considered in the Present Study, and for Both Hemispheres

	Cap	Dawn aurora	Dusk aurora
Northern hemisphere	−0.45	−0.01	−0.09
Southern hemisphere	−0.43	−0.17	−0.22

ing spectra, the spectral index at larger scales, 1.6, closely matches the $\alpha = 5/3 \approx 1.67$ associated with the turbulent cascade theory (Kintner & Seyler, 1985; Mounir et al., 1991). This is indicating that turbulence is dominating over plasma diffusion on scales larger than the breakpoint, and that diffusion takes over for scales smaller than the breakpoint. α_1 for steepening spectra tends to be considerably lower than α_0 for non-steepening spectra.

In panels (d and h) of Figure 2, we see that the location of the spectral break itself occurs more or less uniformly across the available frequency interval for all three regions considered. We note, though, that a semblance of a dual peak distribution can be inferred, with one peak near 10 km and another near 4 km. Furthermore, the long-term SSI development inside the polar caps (Figure 2, panel j) reflects the results from Ivarsen et al. (2019), though with a clearer solar cycle trend. The solid lines, which are linear fits of raw SSI against SZA (Equation 5), vary in near perfect unison, showing clearly that the polar cap SSI seasonal dependencies are driven by incident solar illumination, which together with the relative invariance of the spectral break location implies that the source of the irregularities present remains unchanged throughout the year. A direct quantification of these dependencies is possible, through the calculation of the point biserial correlation between SZA and SSI, for the entire data set of 7 million steepening slope classifications. The point biserial correlation coefficient is the equivalent of the Pearson correlation coefficient for association between a continuous and a binary variable (Kornbrot, 2014). We show this correlation coefficient in Table 1. The point biserial correlation between SZA and SSI is −0.45, −0.01, and −0.09, for the cap, dawn aurora, and dusk aurora respectively, for the northern hemisphere. For the southern hemisphere, these numbers become −0.43, −0.17, and −0.22, indicating that there is a clear relationship between SZA and SSI in both polar caps, and less so in the auroral regions. For a brief discussion on the solar cycle trend in the long-term polar cap SSI occurrence rate, see the end of this section.

In the general SSI climatology, in Figure 3, and specifically inside the polar caps (poleward of $\sim \pm 82^\circ$ MLAT) in panels (a through f) in Figure 3, we see that the SSI occurrence rate closely follows the sunlight terminators, indicated by the median SZA-values. This provides strong evidence for an SZA-dependence in polar cap plasma irregularity dissipation, due to photoionization-induced enhancements in E-region conductance (Ivarsen et al., 2019; Kivanc & Heelis, 1998). A high ratio of E-to F-region conductance in Equation 2 causes plasma to diffuse with a faster rate owing to the shorting out of electric fields by the E region (Vickrey & Kelley, 1982). Moreover, as is evident in panels (a through d) of Figure 4, summer polar cap SSI occurrence rates are largely independent of geomagnetic conditions. Thus, SZA, or incident sunlight photoionization, is the biggest stakeholder in polar cap SSI occurrence rate, which is reflected in panel (j) of Figure 2 and Table 1.

There is no clear enhancement in SSI occurrence rate in the cusp regions ($\sim \pm 75^\circ$ MLAT and ~ 12 h MLT) in Figures 3–5. Here, a particularly strong and structured injection of auroral precipitation occurs (Jin et al., 2015; Rother et al., 2007). This is reflected by a clear cusp-enhancement in plasma structuring (panels *i* through *m*, Figures 4 and 5). However, cusp particle precipitation, and the dayside diffuse aurora equatorward of the cusp, are associated with a relatively low particle energy (Newell et al., 2010). As such, precipitating electrons here penetrate less deeply, and are expected to structure the ionospheric F-region at km scales (Millward et al., 1999; Rother et al., 2007), while having little effect on the E-region. This means rather than the E-region Pedersen conductance, F-region conductance is directly enhanced by the cusp precipitation, causing the ratio of E-to F-region conductance in Equation 2 to diminish, forcing plasma diffusion to proceed with a slower rate (Vickrey & Kelley, 1982). Depending on the exact location of the cusp, the lack of cusp-associated SSI is discernible both during local summer (panels *a* through *d* of Figure 4), and during local winter (panels *a* through *d* of Figure 5).

In panels (a through d) in Figure 5, at auroral latitudes ($63^\circ < \text{MLAT} < 77^\circ$) at all local times bar the noon-sector, we observe consistently high SSI occurrence rates (>60%). These regions are in deep darkness (right side plots in Figure 3). Looking at the FAC density in panels (e through h) in Figure 5, we identify these regions as the upward dawn-side FAC region 2, and the upward dusk-side region 1, where the former is slightly more equatorward than the latter (Iijima & Potemra, 1978). On the dawn side, the region 2 is dominated by the diffuse aurora (Newell et al., 2010), which occurs primarily on the region 2's closed mag-

netic field lines (Nishimura et al., 2020). The dusk side region 1 is dominated by the discrete aurora (Newell et al., 1996). These two regions of upward flowing FAC are also co-located with the occurrence of GPS phase scintillations (Clausen et al., 2016).

4.2. The Connection Between SSI and E Region Conductance

Given that both the SSI index and the diffusion times have a similar morphology in terms of the presence of a strong E region, we are led to conclude that the reason for the local winter auroral SSI occurrence rates (panels *a* through *d* in Figure 5) is a *precipitation-induced enhancement in E-region Pedersen conductance*. This means that the effect of the E-region enhancement in conductance is twofold. First, it allows the mechanism first proposed by VK82 to operate freely, even under a complete lack of incident sunlight as deeply penetrating particle precipitation in the dark auroral ionosphere brings the ratio $\Sigma_E / (\Sigma_E + \Sigma_F)$ in Equation 2 closer to 1, allowing plasma to diffuse at a higher rate. Second, we have to conclude that because the frequency index undergoes steepening primarily when there is an E-region enhancement in conductance, the implication is that when the E region conductance is important, the spectra are far more likely to steepen. It happens according to the following script: at lower frequencies there is a predominance of turbulent cascading. At frequencies beyond the break point, the power goes down more steeply. In Figure 6 we use a stack of contour plots to present added details about the relation between the spectral power density, the value of α_2 , and the wavelength of the structures for all the cases covered in Figures 4 and 5. The plots of Figure 6 have several remarkable features. One is that for a given wavelength the statistics do not depend at all on whether or not the data were acquired in the polar cap or in the dusk or dawn auroras. Also, there is a lot of similarity between the forms of the plots related to the individual sizes of the structures, although there is some visible evolution in relation to the smaller spectral power and smaller α_2 region. The result is that when a linear regression is applied to the data set in each panel, there is a decreasing correlation coefficient between spectral power and α_2 . One more noticeable feature is that there is less average power at the smaller wavelengths, particularly for wavelengths smaller than 5 km. This is consistent with the cascading context in that in ordinary cascade there is more energy at larger wavelengths. That same cascading concept is related to the frequency spectrum at a given wavelength: aside from spontaneous growth or decay occurring at a given wavelength, wave energy found at one size is assumed to be fed by larger structures and given to smaller ones. In that context the presence of steepening under high E-region density conditions indicates that all wavelengths in the sampled 1–100 km range are subject to increased spontaneous decay when the E region conductance is elevated.

The above notwithstanding, we observe elevated SSI occurrence rates at all local times associated with the discrete and diffuse aurora, but more so in the dawn side diffuse aurora. The reason for this dawn-dusk asymmetry has to lie in key differences between the two categories of aurora that influence SSI occurrence rates. The diffuse aurora is the dominant source of auroral energy (Newell et al., 2009), and is characterized by high-energy precipitation (Nishimura et al., 2020). The pulsating aurora is a subcategory of the diffuse aurora, and it supports especially high-energy precipitating electrons, with characteristic particle energies on the order of several keV and higher (Bryant et al., 1975; Miyoshi et al., 2010, 2020; Nishimura et al., 2020). Such high-energy precipitation will promptly penetrate deep into the ionosphere (Brown et al., 1976; Partamies et al., 2017), reaching the E-region peak at 110 km. This is shown in a study by Kwak and Richmond (2007), where the early morning E-region enhancement in Pedersen conductivity can be deduced to follow from deeply penetrating electrons (Coumans et al., 2004; Vickrey et al., 1981). The *discrete* aurora is characterized by particle energies lower than that of the diffuse aurora (Liou et al., 1997; Lyons & Evans, 1984; Newell et al., 1996; Shue et al., 2001). Furthermore, the overall energy flux of discrete aurora is lower than that of the diffuse aurora (Newell et al., 2009). The former can then induce less change to the Pedersen conductance than the latter, as exemplified in a recent study by Robinson et al. (2021). The dawn-dusk asymmetry seen in panels (a through d) in Figure 5 is then a consequence of these considerations.

However, as mentioned, the strong co-location between both the discrete and the diffuse aurora in panels (a through d) in Figure 5 can conceivably also be interpreted in the context of *energy injection* in the steepening slope spectra (Kintner & Seyler, 1985; Mounir et al., 1991). In this context, a spectral break would be indicative of turbulent structuring rather than the presence of dissipation. However, as a counterpoint, we are not observing any clear cusp-region enhancement in SSI occurrence rates, despite evidence of strong

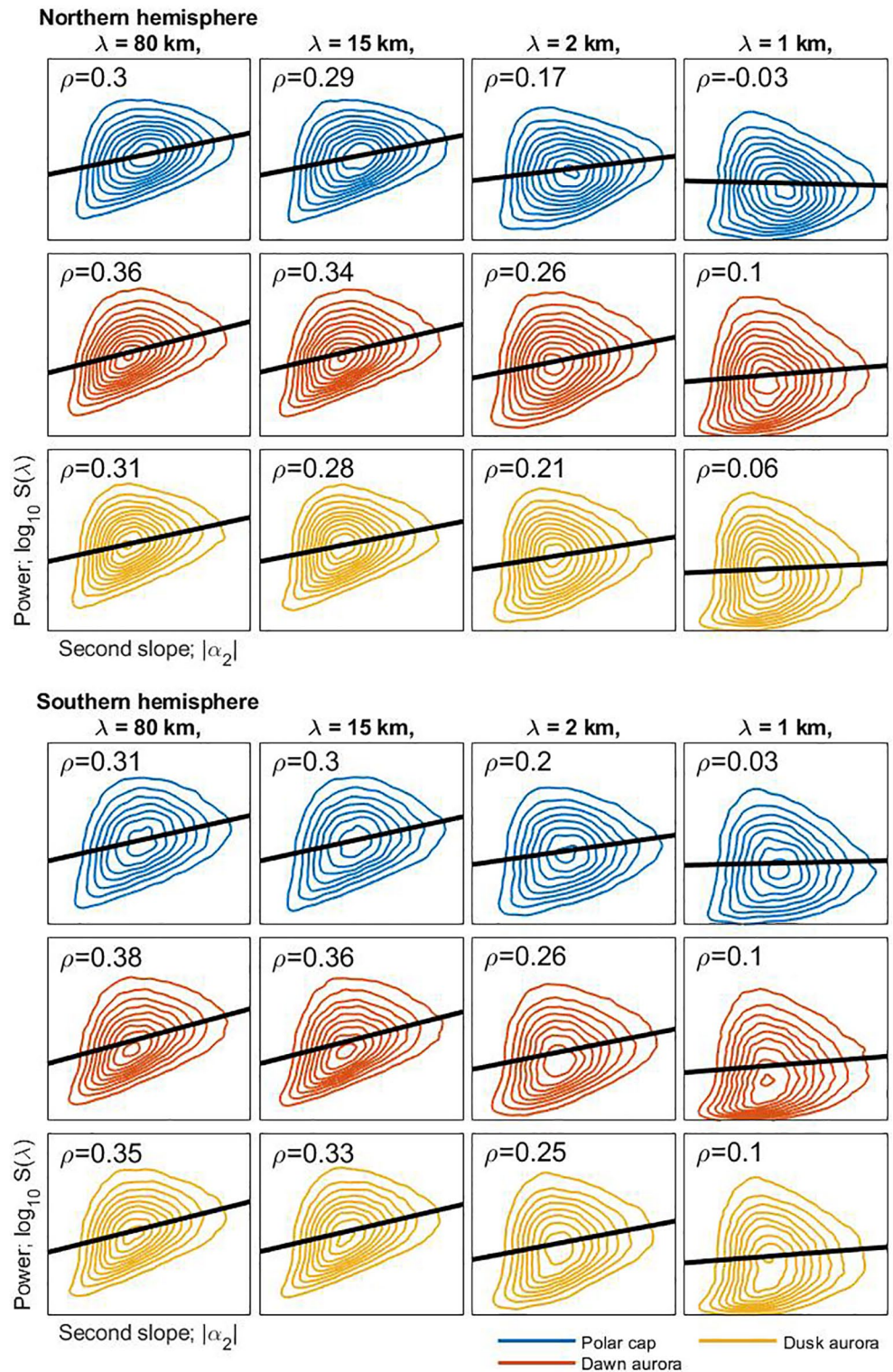


Figure 6. Contour lines based on 2D histograms of $\log_{10} S$ (y -axis) against $|\alpha_2|$ (x -axis) for four scales, with the scales indicated by λ . Also indicated in each panel is the scale-dependent Pearson correlation based on simple linear regressions. Each row corresponds to one of the three regions of interest (indicated by color, see legend below the figure), and the top 12 panels contain data from the northern hemisphere, while the bottom 12 panels contain data from the southern hemisphere.

plasma structuring there ([Jin et al., 2015] [Rother et al., 2007], and panels i through m of Figures 4 and 5 in the present study). To complicate matters further, plasma turbulence leads to enhanced mixing, causing unstable plasma to undergo an accelerated return to equilibrium, perhaps through Bohm diffusion (Braginskii, 1965; Kaufman, 1990). In that case, fast evolving structures can undergo rapid growth and corresponding rapid dissipation (St-Maurice & Hamza, 2009), which likewise would translate to an increase in the SSI occurrence rate. Finally, steepening plasma density spectra has been found in the cusp, but with break points at much lower scales than the Swarm data can resolve (Spicher et al., 2014).

In summary, during local winter, we observe strong co-location between the discrete and pulsating aurora, and regions of enhanced SSI occurrence rates. We interpret this in two ways. First, the framework developed by VK82 (Equation 2) provides an avenue for deeply penetrating precipitation to directly modulate plasma irregularity dissipation: high-energy deeply penetrating precipitation will raise Σ_E , and thus *increase* topside plasma irregularity dissipation. Conversely, lower energy precipitation will penetrate less deeply, and raise Σ_F , which will in turn *decrease* the rate of topside plasma irregularity dissipation. Second, the presence of plasma turbulence can induce spectral breaks, increasing SSI occurrence rates in regions rich in energy injection through particle precipitation, and plasma turbulence can itself lead to anomalous diffusion. Together, these considerations explain how the occurrence of steepening slope spectra during local winter is intimately connected with particle precipitation. While the local summer aurora features a higher number flux, particle energies are lower (Hamrin et al., 2005; Newell et al., 2010). This, and the abundance of solar EUV photoionization in the auroral region during local summer, means that the intimate relationship between break-points in plasma density spectra and particle precipitation is a winter phenomenon.

The local winter dynamics between particle precipitation and irregularity dissipation might have widespread consequences for how we understand F-region auroral plasma irregularities. At auroral latitudes during local winter, SSI can serve as a placeholder for the existence of particle precipitation in Swarm-sampled plasma. Furthermore, given a fuller understanding of precipitation-induced energy injection, analyses of break-points in plasma density spectra can give observational constraints on the distribution of high-latitude E-region conductance. This method can work in synergy with other methods of diagnosing ionospheric conductances, which could be based on ionospheric reflection coefficients (e.g., Ivarsen et al., 2020; Pakhotin et al., 2018), or on global FAC density maps ((Robinson et al., 2021), and references therein).

4.3. What Causes the Mapping Between Swarm Altitude and the E Region

Our results clearly indicate that the evolution of F region structures depends on the E region plasma density, even for wavelengths as small as 1 km. This is somewhat unexpected, based on the consideration of expected parallel to Pedersen conductivity ratios (Heelis & Vickrey, 1990). We have therefore revisited this question in Appendix B through a calculation of typical conductivity ratios encountered in our study and their impact on the mapping scales. We have also queried the effect of gradients in the parallel conductivity. We show in the Appendix that the conductivity ratio is large enough for 1 km structures to map down to 200 km altitude. Below that altitude, we require the impact of the conductivity gradient to allow the mapping to extend all the way to the lower E region. We suggest that the combined action of large conductivity gradients at high latitudes and of the impact of gradients in the parallel conductivity below the F peak are able to explain why we find the E region conductance to have an impact on structures as small as 1 km that are observed at Swarm altitudes.

4.4. Inter Hemispheric Asymmetries

There is a need to discuss briefly the hemispheric asymmetry evident in the SSI occurrence rates (panels a through d, in Figure 5), where the northern hemisphere local winter is characterized by markedly higher SSI occurrence rates. There are two underlying asymmetries at play. First, there is a large distance between the geographic and geomagnetic south poles (Jin & Xiong, 2020), causing the southern hemisphere polar region to exhibit a wider range of SZA values than in the northern hemisphere. Second, recent studies have found that the northern hemisphere is characterized by stronger field-aligned currents that cannot be explained by differing SZA distribution (Ivarsen et al., 2020; Workayehu et al., 2020), as well as stronger energy input in the form of Poynting flux (Pakhotin et al., 2021). As we have shown, during local winter,

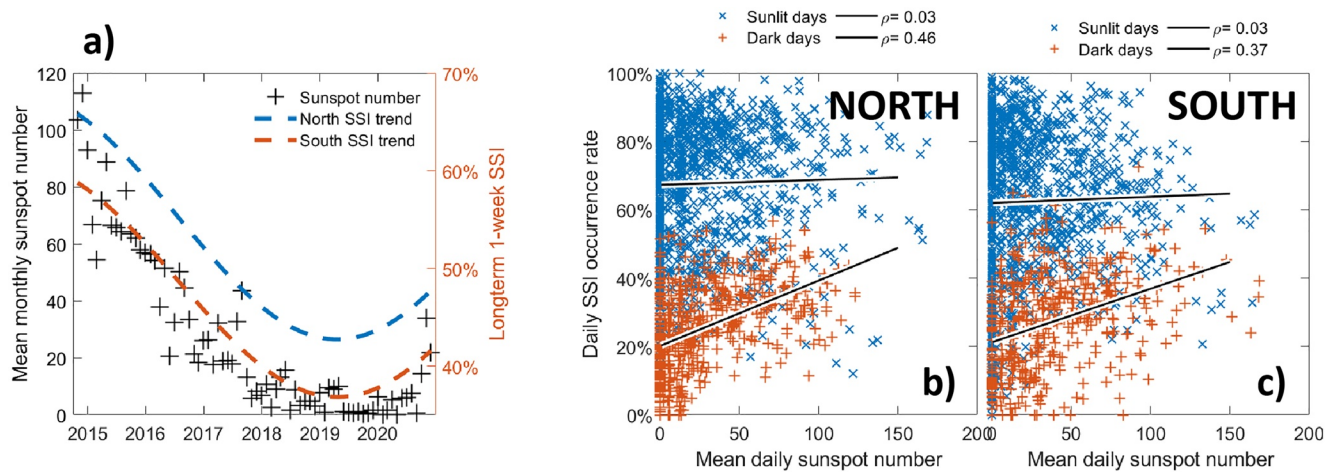


Figure 7. Solar cycle trends in the SSI. Panel (a) shows mean monthly sunspot number along the left y -axis (black crosses), and the solar cycle-based long-term SSI trend along the right y -axis (dashed lines), where the northern hemisphere is shown in blue, and the southern hemisphere in orange. Panels (b and c) show daily SSI occurrence rate inside the polar caps (poleward of $\pm 82^\circ$ MLAT) along the y -axis, and mean daily sunspot number along the x -axis. The data is divided into days with a median SZA $< 90^\circ$ (sunlit days, blue), and days with a median SZA $> 90^\circ$ (dark days, orange). The Pearson correlation coefficients for linear regressions done on both groups are indicated, and the linear fits plotted with black solid lines. Panel (b) shows the northern hemisphere, and panel (c) the southern hemisphere.

SSI occurrence rates are dependent on auroral particle precipitation, and so the local winter hemispheric asymmetry in SSI occurrence rates should be seen in this context. To quantify the hemispheric asymmetry that is due to different SZA distributions, we refer to the point biserial correlation coefficient between SZA and SSI in Table 1. We see that while the correlation between SZA and SSI is negligible in the northern auroral regions, it is considerably stronger in the southern auroral region. While the stronger SZA-SSI correlation in the southern auroral region could be a direct result of the wide range of SZA values there, the greater influence of particle precipitation on northern SSI occurrence rates could also contribute to a lower SZA-SSI correlation in the northern auroral region. A discussion of the hemispheric asymmetry in high-latitude plasma structuring is outside the scope of the present study (see, e.g. Jin & Xiong, 2020) for a recent investigation into hemispheric asymmetries in plasma density).

4.5. Solar Cycle Effects

We conclude this section with a brief discussion of the solar cycle trend discernable in the long term polar cap SSI occurrence rate (panel j of Figure 2). In the model presented in Equation 5, we add a slow cyclical variation in the long-term SSI occurrence rate. This slow variation, $p_{SC}(t)$, is shown in panel (a) of Figure 7, which shows mean monthly sunspot number on the left y -axis, and $p_{SC}(t) + \bar{p}$ along the right y -axis, where \bar{p} is the overall median 1-week polar cap SSI occurrence rate (see Appendix A for details about $p_{SC}(t)$). To estimate solar activity, we use sunspot data from the World Data Center SILSO, Royal Observatory of Belgium, Brussels. The solar cycle dependence in the long-term polar cap SSI is, however, not fully captured by a simple cyclical variation. In panels (b and c) in Figure 7, we show scatter plots of daily polar cap SSI occurrence rate against mean daily sunspot number, with blue datapoints representing days on which the median SZA $< 90^\circ$, and red datapoints representing days on which the median SZA $> 90^\circ$. Note that while the SSI data in panel (a) is based on 1-week occurrence rates, the SSI data in panels (b and c) is based on 1-day occurrence rates. The two categories in panels (b and c) show drastically differing behavior with respect to sunspot number, exemplified by the Pearson correlation coefficient in the two categories (indicated above the plots). Days during which the polar caps are on average sunlit exhibit no dependence on solar activity. Conversely, days during which the polar caps on average receive no incident sunlight, exhibit a clear dependence on solar activity, with Pearson correlation coefficients of 0.46 (for the northern hemisphere) and 0.37 (southern hemisphere). In fact, days with very low polar cap SSI occurrence rate ($< 10\%$) exclusively occur on days with comparatively low solar activity. The fact that SSI occurrence rate in the sunlit polar cap does not depend on sunspot numbers while that in the dark polar cap does, reflects the

two stakeholders in steepening plasma density spectra: in the presence of solar illumination, geomagnetic influence on SSI occurrence rate is suppressed, as SSI occurrence rates are generally high. In that case, solar photoionization is the main stakeholder in SSI occurrence rate. In the absence of solar illumination, the geomagnetic influence on SSI occurrence rates is substantial, with auroral particle precipitation being the main stakeholder in SSI occurrence rate.

5. Conclusion

We have calculated and collected seven million plasma density spectra measured by Swarm A. Based on an analysis of the Swarm 16 Hz Advanced Plasma Density data set, and, utilizing an automatic detection of spectral breaks, we present a comprehensive climatology of the occurrence of break-points and subsequent steepening in plasma density spectra at high latitudes. Steepening density spectra tend to exhibit a spectral index of 1.6 at larger scales throughout the high-latitude F-region ionosphere, indicating that turbulence is ubiquitous. The steepening itself shows that turbulence goes hand in hand with VK82-style irregularity dissipation.

At auroral latitudes, we have shown that deeply penetrating particle precipitation is facilitating irregularity dissipation described by the VK82 framework. Here, we see a picture of a complicated synergy between dissipation and turbulence, and this causes the steepening slope index, SSI, to act as a placeholder for the prevalence of auroral particle precipitation. Conversely, near the cusp, an enhancement in F-region conductance, as opposed to E-region conductance, is inhibiting irregularity dissipation.

Although the fact that the nightside aurora can modulate ionospheric conductivity has previously been recognized (Shue et al., 2001, e.g.), measuring the aurora-induced conductivity has proven to be exceedingly difficult (Weimer & Edwards, 2021). Our results indicate that electron precipitation from the diffuse and discrete aurora are strongly enhancing E-region conductance, causing widespread irregularity dissipation in the local winter auroral region. That the framework developed by VK82 has been given an avenue to work in complete darkness invites an entirely new discussion of how particle precipitation can structure the local winter high-latitude F-region ionosphere.

It should be kept in mind that the spectral interval available to scrutiny in the present study is limited. Break-points can naturally be found on multiple scales outside the interval under consideration. In fact, in-situ experiments have documented spectral breaks on much smaller scales than those encountered in the present study (Basu et al., 1990; Mounir et al., 1991; Spicher et al., 2014). Likewise, high-frequency radar experiments can monitor decameter scale plasma fluctuations in the ionosphere, where some statistical studies show enhanced spectral broadening on auroral latitudes (Villain et al., 2002). The spectral breaks documented in the present study might be linked to structuring at much smaller scales through turbulent cascade, highlighting an avenue for future applications for the SSI.

Appendix A: Polar Cap SSI Model Parameters

The SSI model shown in Equation 5 consists of a linear fit of SSI against SZA, for all seven million spectra, and a slowly varying solar cycle-based trend. The former, p_{SZA} is determined by linear regression,

$$p_{\text{SZA}}(Z) = \begin{cases} 158 - 0.013 \times Z, & \text{for the northern hemisphere,} \\ 143 - 0.011 \times Z, & \text{for the southern hemisphere.} \end{cases} \quad (\text{A1})$$

For the slowly varying solar cycle component, p_{SC} , we find that the following function accurately describes the deviations from the long-term median in the polar cap SSI occurrence rate,

$$p_{\text{SC}} = \frac{\sigma}{2} \sin\left(\frac{2\pi}{11 \text{ years}} \times t + \theta_0\right), \quad (\text{A2})$$

where σ is the standard deviation of the long term 1-week polar cap SSI occurrence rate, t is the number of days elapsed since 0 January year 0, and θ_0 is a phase shift that aligns the solar minimum near the end of 2019. In practice, Equation A2 becomes,

$$p_{\text{SC}} = \begin{cases} 12.6 \sin(0.0016 \times t + 0.34), & \text{for the northern hemisphere,} \\ 12.0 \sin(0.0016 \times t + 0.34), & \text{for the southern hemisphere.} \end{cases} \quad (\text{A3})$$

The result is displayed in panel (a) of Figure 7, which shows $\bar{p} + p_{\text{SC}}$ along the right y-axis, where \bar{p} is the long-term median polar cap SSI occurrence rate. Note that the unit for (Equations A1–A3) is percentage occurrence rate.

Appendix B: The Coupling Between E and F Region Plasma Structures

In a simple yet powerful argument Farley (1959) used the null current divergence condition from which we can infer that structures less than around 10 km in size should not map over more than 200 km in altitude. However, we have found clear evidence for the fact that even sub-km size structures at 450 km altitude are affected by the conductivity of the E region. In this appendix, we revisit the Farley argument based on typical sets of conditions met in our study. We also argue that for the altitudes of interest in the present work, the vertical derivative of the parallel conductivity could play an important role so that smaller scales than inferred from the original Farley paper could map from 450 km down to 100 km altitude. As with the original study by Farley (1959), our analysis of the extra conductivity gradient contribution is strictly based on dimensional analysis, meaning that it does not deal with actual solutions to the relevant differential equation.

Following Farley (1959), we start with the null current divergence condition. Being interested in perpendicular diffusion, we Fourier analyze the structures in the plane perpendicular to the magnetic field. We retain only parallel and Pedersen currents and use $\mathbf{E} = -\nabla\Phi$, where \mathbf{E} is the ionospheric electric field and Φ is the associated electric potential. Furthermore, we drop gradients in the ambient Pedersen conductivity owing to the scales under consideration, and we assume the magnetic field to be vertical to leading order. The current continuity then becomes,

$$-k_{\perp}^2 \sigma_{\perp} \Phi + \frac{\partial \sigma_{\parallel}}{\partial z} \frac{\partial \Phi}{\partial z} + \sigma_{\parallel} \frac{\partial^2 \Phi}{\partial z^2} = 0, \quad (\text{B1})$$

where $k_{\perp} = 2\pi / \lambda_{\perp}$ and σ_{\parallel} is the parallel conductivity. It is to be understood that Φ is the k -component of the Fourier analyzed potential and that we are after its variation along the vertical direction z . After dividing by σ_{\parallel} we end up with the equation,

$$\frac{\partial^2 \Phi}{\partial z^2} + \frac{\partial \ln \sigma_{\parallel}}{\partial z} \frac{\partial \Phi}{\partial z} - k_{\perp}^2 \frac{\sigma_{\perp}}{\sigma_{\parallel}} \Phi = 0. \quad (\text{B2})$$

Above about 200 km altitude σ_{\parallel} is mainly proportional to the plasma density while below 200 km it is mainly proportional to the neutral density. We should therefore use

$$\frac{\partial \ln \sigma_{\parallel}}{\partial z} \approx -\frac{1}{H}, \quad (\text{B3})$$

where H is of the order of the neutral scale height below 200 km and of the order of the ion scale height above 200 km (although it should be kept in mind that the plasma density normally tends to increase between 200 and 300 km altitudes).

If the derivative of the parallel conductivity is ignored we end up with the potential having an exponential decay of the form $\Phi_0 \exp(-z / \Delta z)$ where $\Delta z = \sqrt{\sigma_{\parallel} / \sigma_p} / k_{\perp}$, as argued by Farley (1959). We note that $\sqrt{\sigma_{\parallel} / \sigma_p} / k_{\perp}$ is inversely proportional to the square root of the plasma density as a function of altitude. Specifically, classical theory gives $\sigma_{\parallel} / \sigma_p = (1 + \nu_i^2 / \Omega_i^2) (\Omega_e \Omega_i) / (\nu_e \nu_i)$, which is normally thought to be of the order of 10^5 to 10^6 at Swarm altitudes (Kelley, 1989b). The net result as described by Farley (1959) is that

structures with a wavelength less than 10 km might or might not map to the E region from Swarm altitudes, although this result would vary with neutral and plasma density conditions.

At the extreme where the wavenumber would be too small to matter in Equation B2 we would find two solutions: one would be $\partial\phi / \partial z = 0$, meaning no parallel electric field at all. The other would describe an electric field that grows exponentially with altitude as the plasma density decreases with the plasma scale height, that is, the scale height of the conductivity.

In actual situations we should be concerned with the competition between all the various terms in Equation B2. Our dimensional analysis ends up with a quadratic equation for $1 / \Delta z$ (Δz being the vertical scaling) in terms of the other parameters. The two possible scales are given by the quadratic solution,

$$\frac{2}{\Delta z} = \frac{1}{H} \pm \frac{1}{H} \sqrt{1 + 4k_{\perp}^2 \frac{H^2}{R}} \quad (\text{B4})$$

where,

$$R = \frac{\sigma_{\parallel}}{\sigma_{\perp}}. \quad (\text{B5})$$

In Equation B4, we have to rule out the solution with the + sign, since it leads to infinite electric fields at infinity, which cannot be satisfied. The other scale would infer a potential (and therefore a parallel electric field) that decreases with increasing altitude, which is what we are looking for. In Figure B1, we show example height profiles for the conductivities under consideration, along with selected solutions to Equation B4. In panel (a), we plot parallel and Pedersen conductivity height profiles for typical high latitude (75° MLAT) conditions, based on global ionospheric models [see Ivarsen et al. (2021), and references therein]. In panel (b), we show the ratio R (Equation B5) along with the logarithmic gradient of the parallel conductivity

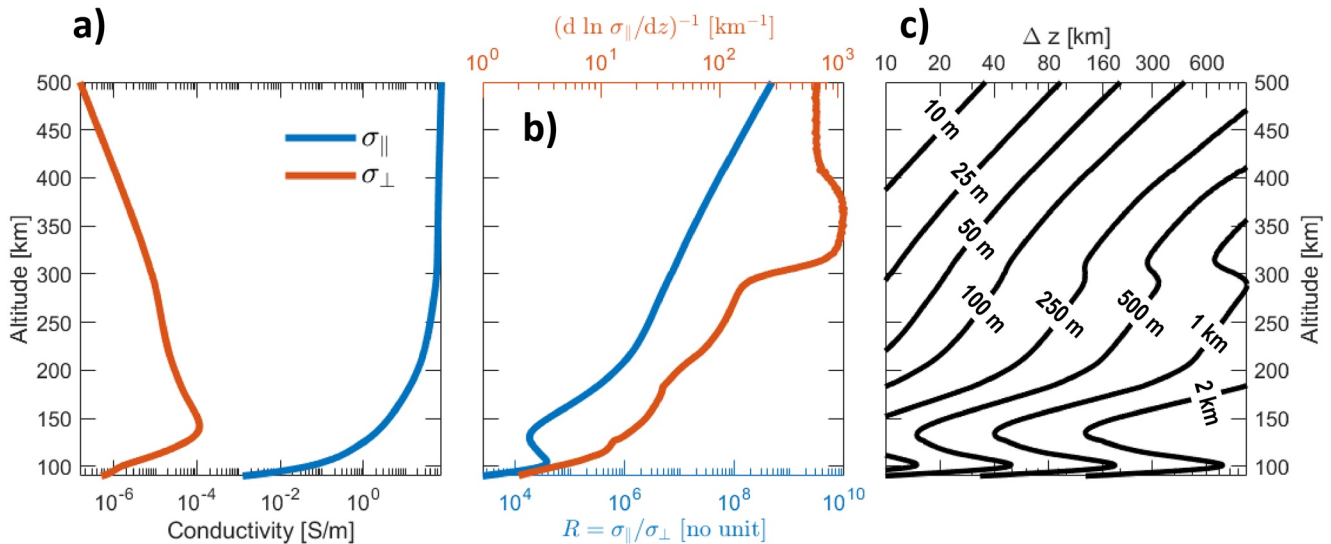


Figure B1. Solving Equation B4 for typical high-latitude ionospheric conditions. Panel (a) shows the height profiles of both parallel and Pedersen conductivities, while panel (b) shows the conductivity ratio R (Equation B5) on the bottom x -axis and $-H$ (Equation B3) on the top x -axis. Panel (c) shows solutions to Equation B4, taking the minus sign, for eight perpendicular irregularity scale lengths λ_{\perp} , indicated in the plot.

$-1 / H$. The values in panels (a and b) are used to produce solutions to Equation B4, taking the minus sign. These are shown in panel (c), for eight values of the perpendicular irregularity scale λ_{\perp} (indicated in the plot). Observe that the ratio R is found to be as large as 10^8 at Swarm altitudes. Along with values of H on the

order of 10^2 – 10^3 at Swarm altitudes, we find that the vertical scaling Δz is sufficiently long for even $\lambda_{\perp} = 100$ m, indicating that km-scaled irregularities would map to the E-region without trouble.

Finally it should be kept in mind that since we did not solve Equation B1 but only looked at its scaling, the scaling arguments need to be revisited at the various altitudes. That is, to say, while we could infer that the mapping scale at Swarm altitudes is high enough at km size wavelengths to map well into the E region, we have to keep in mind that by 200 km altitude the scaling changes. This means that the scaling at 200 km must be revisited before concluding that km structures map down by another 100 km or so. This stated, with the numbers found hereby we can safely conclude that km wavelengths do map well between Swarm altitudes and the lower E-region.

Data Availability Statement

Sunspot data are courtesy of SILSO, World Data Center—Sunspot Number and Long-term Solar Observations, Royal Observatory of Belgium, and can be accessed from <http://www.sidc.be/silso/>.

Acknowledgments

This work is a part of the 4DSpace initiative at the University of Oslo, and is supported in part by Research Council of Norway grants 275655, 275653, and 267408, and in part by the European Research Council (ERC) under the European Unions Horizon 2020 research and innovation programme (grant agreement No 866357). The authors acknowledge ESA for the provision of the Swarm data, which was accessed from <https://earth.esa.int/web/guest/swarm/data-access>. The authors gratefully acknowledge the SuperMAG collaborators (<https://supermag.jhuapl.edu/info/?page=acknowledgement>). The authors would like to extend thanks to D. J. Knudsen, J. K. Burchill, and S. C. Buchert for their work on the Swarm Thermal ion imager instrument.

References

- Baker, K. B., & Wing, S. (1989). A new magnetic coordinate system for conjugate studies at high latitudes. *Journal of Geophysical Research*, 94(A7), 9139–9143. <https://doi.org/10.1029/JA094iA07p09139>
- Basu, S., Basu, S., MacKenzie, E., Coley, W. R., Sharber, J. R., & Hoegy, W. R. (1990). Plasma structuring by the gradient drift instability at high latitudes and comparison with velocity shear driven processes. *Journal of Geophysical Research*, 95(A6), 7799–7818. <https://doi.org/10.1029/JA095iA06p07799>
- Bilitza, D., Altadill, D., Zhang, Y., Mertens, C., Truhlik, V., Richards, P., et al. (2014). The International Reference Ionosphere 2012 a model of international collaboration. *Journal of Space Weather and Space Climate*, 4, A07. <https://doi.org/10.1051/swsc/2014004>
- Bilitza, D., & Reinisch, B. W. (2008). International Reference Ionosphere 2007: Improvements and new parameters. *Advances in Space Research*, 42(4), 599–609. <https://doi.org/10.1016/j.asr.2007.07.048>
- Braginskii, S. I. (1965). Transport processes in a plasma. *Reviews of plasma physics*, 1, 205. Retrieved from <http://adsabs.harvard.edu/abs/1965RvPP\dots1\enleadertwodots205B>
- Brekke, A., & Moen, J. (1993). Observations of high latitude ionospheric conductances. *Journal of Atmospheric and Terrestrial Physics*, 55(11), 1493–1512. [https://doi.org/10.1016/0021-9169\(93\)90126-J](https://doi.org/10.1016/0021-9169(93)90126-J)
- Brown, N. B., Davis, T. N., Hallinan, T. J., & Stenbaek-Nielsen, H. C. (1976). Altitude of pulsating aurora determined by a new instrumental technique. *Geophysical Research Letters*, 3(7), 403–404. <https://doi.org/10.1029/GL003i007p00403>
- Bryant, D. A., Smith, M. J., & Courtier, G. M. (1975). Distant modulation of electron intensity during the expansion phase of an auroral substorm. *Planetary and Space Science*, 23(5), 867–878. [https://doi.org/10.1016/0032-0633\(75\)90022-7](https://doi.org/10.1016/0032-0633(75)90022-7)
- Califano, F., Cecchi, T., & Chiuderi, C. (2002). Nonlinear kinetic regime of the Weibel instability in an electronion plasma. *Physics of Plasmas*, 9(2), 451–457. <https://doi.org/10.1063/1.1435001>
- Clausen, L. B. N., Moen, J. I., Hosokawa, K., & Holmes, J. M. (2016). GPS scintillations in the high latitudes during periods of dayside and nightside reconnection. *Journal of Geophysical Research: Space Physics*, 121(4), 3293–3309. <https://doi.org/10.1002/2015JA022199>
- Coumans, V., Grd, J.-C., Hubert, B., Meurant, M., & Mende, S. B. (2004). Global auroral conductance distribution due to electron and proton precipitation from IMAGE-FUV observations. *Annales Geophysicae*, 22(5), 1595–1611. <https://doi.org/10.5194/angeo-22-1595-2004>
- Cowley, S. W. H. (2000). TUTORIAL: Magnetosphere-ionosphere interactions: A tutorial review. In *Washington DC American Geophysical Union geophysical monograph series* (Vol. 118, pp. 91–106). <https://doi.org/10.1029/GM118p0091>
- D'Errico, J. (2017). *SLM—Shape language modeling—File exchange—MATLAB central*. Retrieved from <http://uk.mathworks.com/matlabcentral/fileexchange/24443-slm-shape-language-modeling>
- Davis, T. N., & Sugiura, M. (1966). Auroral electrojet activity index AE and its universal time variations. *Journal of Geophysical Research*, 71(3), 785–801. <https://doi.org/10.1029/JZ071i003p00785>
- Dungey, J. W. (1961). Interplanetary magnetic field and the auroral zones. *Physical Review Letters*, 6, 47–48. <https://doi.org/10.1103/PhysRevLett.6.47>
- Farley, D. T. (1959). A theory of electrostatic fields in a horizontally stratified ionosphere subject to a vertical magnetic field. *Journal of Geophysical Research*, 64(9), 1225–1233. <https://doi.org/10.1029/jz064i009p01225>
- Friis-Christensen, E., Lhr, H., & Hulot, G. (2006). Swarm: A constellation to study the Earth's magnetic field. *Earth, Planets and Space*, 58, 351–358. <https://doi.org/10.1186/BF03351933>
- Fujii, R., Iijima, T., Potemra, T. A., & Sugiura, M. (1981). Seasonal dependence of large-scale Birkeland currents. *Geophysical Research Letters*, 8(10), 1103–1106. <https://doi.org/10.1029/gl008i010p01103>
- Gjerloev, J. W. (2012). The SuperMAG data processing technique. *Journal of Geophysical Research*, 117(A9), A09213. <https://doi.org/10.1029/2012ja017683>
- Grono, E., & Donovan, E. (2020). Surveying pulsating auroras. *Annales Geophysicae*, 38(1), 1–8. <https://doi.org/10.5194/angeo-38-1-2020>
- Hamrin, M., Norqvist, P., Rnnmark, K., & Fellg, D. (2005). The importance of solar illumination for discrete and diffuse aurora. *Annales Geophysicae*, 23(11), 3481–3486. <https://doi.org/10.5194/angeo-23-3481-2005>
- Heelis, R. A., & Vickrey, J. F. (1990). Magnetic field-aligned coupling effects on ionospheric plasma structure. *Journal of Geophysical Research*, 95(A6), 7995–8008. <https://doi.org/10.1029/ja095iA06p07995>
- Heppner, J. P., Liebrecht, M. C., Maynard, N. C., & Pfaff, R. F. (1993). High-latitude distributions of plasma waves and spatial irregularities from DE 2 alternating current electric field observations. *Journal of Geophysical Research*, 98(A2), 1629–1652. <https://doi.org/10.1029/92ja01836>

- Hong, J., Chung, J.-K., Kim, Y. H., Park, J., Kwon, H.-J., Kim, J.-H., et al. (2020). Characteristics of ionospheric irregularities using GNSS scintillation indices measured at Jang Bogo Station, Antarctica (74.62°S, 164.22°E). *Space Weather*, 18(10), e2020SW002536. <https://doi.org/10.1029/2020sw002536>
- Huba, J. D., Hassam, A. B., Schwartz, I. B., & Keskinen, M. J. (1985). Ionospheric turbulence: Interchange instabilities and chaotic fluid behavior. *Geophysical Research Letters*, 12(1), 65–68. <https://doi.org/10.1029/gl012i001p00065>
- Iijima, T., & Potemra, T. A. (1978). Large-scale characteristics of field-aligned currents associated with substorms. *Journal of Geophysical Research*, 83(A2), 599–615. <https://doi.org/10.1029/ja083ia02p00599>
- Ivarsen, M. F., Jin, Y., Spicher, A., & Clausen, L. B. N. (2019). Direct evidence for the dissipation of small-scale ionospheric plasma structures by a conductive E region. *Journal of Geophysical Research: Space Physics*, 124(4), 2935–2942. <https://doi.org/10.1029/2019JA026500>
- Ivarsen, M. F., Jin, Y., Spicher, A., Miloch, W., & Clausen, L. B. N. (2021). The lifetimes of plasma structures at high latitudes. *Journal of Geophysical Research: Space Physics*, 126(2), e2020JA028117. <https://doi.org/10.1029/2020ja028117>
- Ivarsen, M. F., Park, J., Kwak, Y.-S., Jin, Y., Knudsen, D. J., & Clausen, L. B. N. (2020). Observational evidence for the role of hall conductance in Alfvén wave reflection. *Journal of Geophysical Research: Space Physics*, 125(12), e2020JA028119. <https://doi.org/10.1029/2020ja028119>
- Jin, Y., Miloch, W. J., Moen, J. I., & Clausen, L. B. N. (2018). Solar cycle and seasonal variations of the GPS phase scintillation at high latitudes. *Journal of Space Weather and Space Climate*, 8, A48. <https://doi.org/10.1051/swsc/2018034>
- Jin, Y., Moen, J. I., & Miloch, W. J. (2015). On the collocation of the cusp aurora and the GPS phase scintillation: A statistical study. *Journal of Geophysical Research: Space Physics*, 120(10), 9176–9191. <https://doi.org/10.1002/2015ja021449>
- Jin, Y., Spicher, A., Xiong, C., Clausen, L. B. N., Kervalishvili, G., Stolle, C., & Miloch, W. J. (2019). Ionospheric plasma irregularities characterized by the swarm satellites: Statistics at high latitudes. *Journal of Geophysical Research: Space Physics*, 124(2), 1262–1282. <https://doi.org/10.1029/2018ja026063>
- Jin, Y., & Xiong, C. (2020). Interhemispheric asymmetry of large-scale electron density gradients in the polar cap ionosphere: UT and seasonal variations. *Journal of Geophysical Research: Space Physics*, 125(2), e2019JA027601. <https://doi.org/10.1029/2019ja027601>
- Kaufman, H. R. (1990). Explanation of Bohm diffusion. *Journal of Vacuum Science and Technology B: Microelectronics Processing and Phenomena*, 8(1), 107–108. <https://doi.org/10.1116/1.584855>
- Kelley, M. C. (1989a). Chapter 2—Fundamentals of ionospheric plasma dynamics. In Kelley, M. C. (Ed.), *The Earth's ionosphere* (pp. 23–63). Academic Press. <https://doi.org/10.1016/b978-0-12-404013-7.50007-1>
- Kelley, M. C. (1989b). Chapter 3—Electrodynamics of the equatorial zone. In Kelley, M. C. (Ed.), *The Earth's ionosphere* (pp. 65–111). Academic Press. <https://doi.org/10.1016/b978-0-12-404013-7.50008-3>
- Kelley, M. C., Vickrey, J. F., Carlson, C. W., & Torbert, R. (1982). On the origin and spatial extent of high-latitude F region irregularities. *Journal of Geophysical Research*, 87(A6), 4469–4475. <https://doi.org/10.1029/ja087ia06p04469>
- Keskinen, M. J., & Huba, J. D. (1990). Nonlinear evolution of high-latitude ionospheric interchange instabilities with scale-size-dependent magnetospheric coupling. *Journal of Geophysical Research*, 95(A9), 15157–15166. <https://doi.org/10.1029/ja095ia09p15157>
- Kintner, P. M., Ledvina, B. M., & de Paula, E. R. (2007). GPS and ionospheric scintillations. *Space Weather*, 5(9). <https://doi.org/10.1029/2006sw000260>
- Kintner, P. M., & Seyler, C. E. (1985). The status of observations and theory of high latitude ionospheric and magnetospheric plasma turbulence. *Space Science Reviews*, 41(1–2), 91–129. <https://doi.org/10.1007/bf00241347>
- Kivanc, O., & Heelis, R. A. (1998). Spatial distribution of ionospheric plasma and field structures in the high-latitude F region. *Journal of Geophysical Research*, 103, 6955–6968. <https://doi.org/10.1029/97ja03237>
- Knudsen, D. J., Burchill, J. K., Buchert, S. C., Eriksson, A. I., Gill, R., Wahlund, J.-E., & Moffat, B. (2017). Thermal ion imagers and Langmuir probes in the Swarm electric field instruments. *Journal of Geophysical Research: Space Physics*, 122(2). <https://doi.org/10.1002/2016ja022571>
- Kornbrot, D. (2014). Point biserial correlation. In *Wiley StatsRef: Statistics reference online*. American Cancer Society. <https://doi.org/10.1002/9781118445112.stat06227>
- Kwak, Y.-S., & Richmond, A. D. (2007). An analysis of the momentum forcing in the high-latitude lower thermosphere. *Journal of Geophysical Research*, 112(A1), A01306. <https://doi.org/10.1029/2006ja011910>
- Liou, K., Newell, P. T., & Meng, C.-I. (2001). Seasonal effects on auroral particle acceleration and precipitation. *Journal of Geophysical Research*, 106(A4), 5531–5542. <https://doi.org/10.1029/1999ja000391>
- Liou, K., Newell, P. T., Meng, C.-I., Brittnacher, M., & Parks, G. (1997). Synoptic auroral distribution: A survey using Polar ultraviolet imagery. *Journal of Geophysical Research*, 102(A12), 27197–27205. <https://doi.org/10.1029/97ja02638>
- Lyons, L. R., & Evans, D. S. (1984). An association between discrete aurora and energetic particle boundaries. *Journal of Geophysical Research*, 89(A4), 2395–2400. <https://doi.org/10.1029/ja089ia04p02395>
- Millward, G. H., Moffett, R. J., Balmforth, H. F., & Rodger, A. S. (1999). Modeling the ionospheric effects of ion and electron precipitation in the cusp. *Journal of Geophysical Research*, 104(A11), 24603–24612. <https://doi.org/10.1029/1999ja000249>
- Miyoshi, Y., Katoh, Y., Nishiyama, T., Sakanoi, T., Asamura, K., & Hirahara, M. (2010). Time of flight analysis of pulsating aurora electrons, considering wave-particle interactions with propagating whistler mode waves. *Journal of Geophysical Research*, 115(A10), A10312. <https://doi.org/10.1029/2009ja015127>
- Miyoshi, Y., Saito, S., Kurita, S., Asamura, K., Hosokawa, K., Sakanoi, T., et al. (2020). Relativistic electron microbursts as high-energy tail of pulsating aurora electrons. *Geophysical Research Letters*, 47(21), e2020GL090360. <https://doi.org/10.1029/2020gl090360>
- Mounir, H., Berthelier, A., Cerisier, J. C., Lagoutte, D., & Beghin, C. (1991). The small-scale turbulent structure of the high latitude ionosphere—Arcad-Aureol-3 observations. *Annales Geophysicae*, 9, 725–737. Retrieved from <http://adsabs.harvard.edu/abs/1991AnGeoI...9...725M>
- Newell, P. T., & Gjerloev, J. W. (2011). Evaluation of SuperMAG auroral electrojet indices as indicators of substorms and auroral power. *Journal of Geophysical Research*, 116(A12), A12211. <https://doi.org/10.1029/2011ja016779>
- Newell, P. T., Lyons, K. M., & Meng, C.-I. (1996). A large survey of electron acceleration events. *Journal of Geophysical Research: Space Physics*, 101(A2), 2599–2614. <https://doi.org/10.1029/95ja03147>
- Newell, P. T., Sotirelis, T., & Wing, S. (2009). Diffuse, monoenergetic, and broadband aurora: The global precipitation budget. *Journal of Geophysical Research*, 114(A9), A09207. <https://doi.org/10.1029/2009ja014326>
- Newell, P. T., Sotirelis, T., & Wing, S. (2010). Seasonal variations in diffuse, monoenergetic, and broadband aurora. *Journal of Geophysical Research*, 115(A3), A03216. <https://doi.org/10.1029/2009ja014805>
- Nishimura, Y., Lessard, M. R., Katoh, Y., Miyoshi, Y., Grono, E., Partamies, N., et al. (2020). Diffuse and pulsating aurora. *Space Science Reviews*, 216(1), 4. <https://doi.org/10.1007/s11214-019-0629-3>

- Pakhotin, I. P., Mann, I. R., Lysak, R. L., Knudsen, D. J., Gjerloev, J. W., Rae, I. J., et al. (2018). Diagnosing the role of Alfv waves in magnetosphere-ionosphere coupling: Swarm observations of large amplitude nonstationary magnetic perturbations during an interval of northward IMF. *Journal of Geophysical Research: Space Physics*, *123*(1), 326–340. <https://doi.org/10.1002/2017ja024713>
- Pakhotin, I. P., Mann, I. R., Xie, K., Burchill, J. K., & Knudsen, D. J. (2021). Northern preference for terrestrial electromagnetic energy input from space weather. *Nature Communications*, *12*(1), 199. <https://doi.org/10.1038/s41467-020-20450-3>
- Partamies, N., Whiter, D., Kadokura, A., Kauristie, K., Tyssy, H. N., Massetti, S., et al. (2017). Occurrence and average behavior of pulsating aurora. *Journal of Geophysical Research: Space Physics*, *122*(5), 5606–5618. <https://doi.org/10.1002/2017ja024039>
- Phelps, A. D. R., & Sagalyn, R. C. (1976). Plasma density irregularities in the high-latitude top side ionosphere. *Journal of Geophysical Research*, *81*(4), 515–523. <https://doi.org/10.1029/ja081i004p00515>
- Picone, J. M., Hedin, A. E., Drob, D. P., & Aikin, A. C. (2002). NRLMSISE-00 empirical model of the atmosphere: Statistical comparisons and scientific issues. *Journal of Geophysical Research*, *107*(A12), SIA15–1–SIA15–16. <https://doi.org/10.1029/2002ja009430>
- Prikryl, P., Jayachandran, P. T., Chadwick, R., & Kelly, T. D. (2015). Climatology of GPS phase scintillation at northern high latitudes for the period from 2008 to 2013. *Annales Geophysicae*, *33*(5), 531–545. <https://doi.org/10.5194/angeo-33-531-2015>
- Ridley, A. J., Gombosi, T. I., & DeZeeuw, D. L. (2004). Ionospheric control of the magnetosphere: Conductance. *Annales Geophysicae*, *22*(2), 567–584. <https://doi.org/10.5194/angeo-22-567-2004>
- Robinson, R. M., Zanetti, L., Anderson, B., Vines, S., & Gjerloev, J. (2021). Determination of auroral electrodynamic parameters from AMPERE field-aligned current measurements. *Space Weather*, e2020SW002677. <https://doi.org/10.1029/2020SW002677>
- Rother, M., Schlegel, K., & Lhr, H. (2007). CHAMP observation of intense kilometer-scale field-aligned currents, evidence for an ionospheric Alfv resonator. *Annales Geophysicae*, *25*(7), 1603–1615. <https://doi.org/10.5194/angeo-25-1603-2007>
- Shue, J.-H., Newell, P. T., Liou, K., & Meng, C.-I. (2001). The quantitative relationship between auroral brightness and solar EUV Pedersen conductance. *Journal of Geophysical Research*, *106*(A4), 5883–5894. <https://doi.org/10.1029/2000ja003002>
- Spicher, A., Miloch, W. J., & Moen, J. I. (2014). Direct evidence of double-slope power spectra in the high-latitude ionospheric plasma. *Geophysical Research Letters*, *41*(5), 1406–1412. <https://doi.org/10.1002/2014gl059214>
- Stenson, E. V., Horn-Stanja, J., Stoneking, M. R., & Pedersen, T. S. (2017). Debye length and plasma skin depth: Two length scales of interest in the creation and diagnosis of laboratory pair plasmas. *Journal of Plasma Physics*, *83*(1). <https://doi.org/10.1017/s0022377817000022>
- St-Maurice, J.-P., & Hamza, A. M. (2009). Small scale irregularities at high latitudes. In Wyman, G. (Ed.), *Characterising the ionosphere* (Technical Report RTO-TR-IST-051). Neuilly-sur-Seine, France: RTO.
- Thult, E., Finlay, C. C., Beggan, C. D., Alken, P., Aubert, J., Barrois, O., & Zvereva, T. (2015). International Geomagnetic Reference Field: The 12th generation. *Earth, Planets and Space*, *67*(1), 79. <https://doi.org/10.1186/s40623-015-0228-9>
- Trbs, M., & Heinzl, G. (2006). Improved spectrum estimation from digitized time series on a logarithmic frequency axis. *Measurement*, *39*(2), 120–129. <https://doi.org/10.1016/j.measurement.2005.10.010>
- Tsunoda, R. T. (1988). High-latitude F region irregularities: A review and synthesis. *Reviews of Geophysics*, *26*(4), 719–760. <https://doi.org/10.1029/rg026i004p00719>
- Vickrey, J. F., & Kelley, M. C. (1982). The effects of a conducting E layer on classical F region cross-field plasma diffusion. *Journal of Geophysical Research*, *87*(A6), 4461–4468. <https://doi.org/10.1029/ja087ia06p04461>
- Vickrey, J. F., Vondrak, R. R., & Matthews, S. J. (1981). The diurnal and latitudinal variation of auroral zone ionospheric conductivity. *Journal of Geophysical Research*, *86*(A1), 65–75. <https://doi.org/10.1029/ja086ia01p00065>
- Villain, J.-P., Andr, R., Pinnock, M., Greenwald, R. A., & Hanuise, C. (2002). A Statistical study of the Doppler spectral width of high-latitude ionospheric F-region echoes recorded with SuperDARN coherent HF radars. *Annales Geophysicae*, *20*(11), 1769–1781. <https://doi.org/10.5194/angeo-20-1769-2002>
- Villain, J. P., Hanuise, C., & Beghin, C. (1986). ARCAD3-SAFARI coordinated study of auroral and polar F-region ionospheric irregularities. *Annales Geophysicae*, *4*, 61–68. Retrieved from <http://adsabs.harvard.edu/abs/1986AnGeo...4...61V>
- Weimer, D., & Edwards, T. (2021). Testing the electrodynamic method to derive height-integrated ionospheric conductances. *Annales Geophysicae*, *39*(1), 31–51. <https://doi.org/10.5194/angeo-39-31-2021>
- Welch, P. (1967). The use of fast Fourier transform for the estimation of power spectra: A method based on time averaging over short, modified periodograms. *IEEE Transactions on Audio and Electroacoustics*, *15*(2), 70–73. <https://doi.org/10.1109/TAU.1967.1161901>
- Workayehu, A. B., Vanham, H., & Aikio, A. T. (2020). Seasonal effect on hemispheric asymmetry in ionospheric horizontal and field-aligned currents. *Journal of Geophysical Research: Space Physics*, *125*, e2020JA028051. <https://doi.org/10.1029/2020JA028051>
- Yamamoto, T., Ozaki, M., & Inoue, S. (2003). Relationship between ionospheric conductivity and intensity of the daytime region 1 field-aligned current in geomagnetically quiet conditions. *Journal of Geophysical Research*, *108*(A5), 1190. <https://doi.org/10.1029/2002ja009607>
- Yeh, K. C., & Liu, C.-H. (1982). Radio wave scintillations in the ionosphere. *IEEE Proceedings*, *70*, 324–360. <https://doi.org/10.1109/proc.1982.12313>